

Uplifting of carbon monoxide from biomass burning and anthropogenic sources to the free troposphere in East Asia

K. Ding^{1,6}, J. Liu^{1,2,6,*}, A. Ding^{1,6}, Q. Liu^{1,6}, T. L. Zhao³, J. Shi⁴, Y. Han¹, H. Wang⁵, F. Jiang⁵

¹School of Atmospheric Sciences, Nanjing University, Nanjing, Jiangsu, 210093, China

²University of Toronto, Toronto, Ontario, M5S 3G3, Canada

³Nanjing University of Information Science & Technology, Nanjing, Jiangsu, 210044, China

⁴Institute of Remote Sensing Applications, Chinese Academy of Sciences, Beijing, 100101, China

⁵International Institute for Earth System Sciences, Nanjing University, Nanjing, Jiangsu, 210093, China

⁶Collaborative Innovation Center of Climate Change, Jiangsu, 210093, China

To: Atmospheric Chemistry and Physics

January 2015

*Corresponding author

1 **Abstract**

2

3 East Asia has experienced rapid development with increasing CO emission in the past
4 decades. Therefore, uplifting CO from the boundary layer to the free troposphere in East
5 Asia can have great implications on regional air quality around the world. It can also
6 influence global climate due to the longer lifetime of CO at higher altitudes. In this study,
7 three cases of high CO episodes in the East China Sea and the Sea of Japan from 2003 to
8 2005 are examined with spaceborne Measurements Of Pollution In The Troposphere
9 (MOPITT) data, in combination with aircraft measurements from the Measurement of
10 Ozone and Water Vapor by Airbus In-Service Aircraft (MOZAIC) program. High CO
11 abundances of 300-550 ppbv are observed in MOZAIC data in the free troposphere
12 during these episodes. These are among the highest CO abundances documented at these
13 altitudes, likely occurring 2-4% in time in the respective altitudes over the region.
14 Correspondingly, elevated CO is shown in MOPITT daytime data in the middle to upper
15 troposphere in the 2003 case, mostly in the lower to middle troposphere in the 2004 case,
16 and in the upper troposphere in the 2005 case. Through analyses of the simulations from
17 a chemical transport model GEOS-Chem and a trajectory dispersion model FLEXPART,
18 we found different CO signatures in the elevated CO and distinct transport pathways and
19 mechanisms for these cases. In the 2003 case, CO from large forest fires near Lake Baikal
20 dominated the elevated CO, which had been rapidly transported upward by a frontal
21 system from the fire plumes. In the 2004 case, anthropogenic CO from the North China
22 Plain experienced frontal lifting and mostly reached ~700 hPa near the East China Sea,
23 while CO from biomass burning from Indochina experienced orographic lifting,

24 leeside-trough induced convection, and frontal lifting through two separate transport
25 pathways, leading to two distinct CO enhancements around 700 hPa and 300 hPa. In the
26 2005 case, high CO of ~300 ppbv, observed in the MOZAIC data around 350 hPa,
27 originated from the anthropogenic source over the vicinity of the Sichuan basin and
28 biomass burning from Indochina, after convection and strong frontal lifting. These cases
29 show that topography affects vertical transport of CO in East Asia via different ways,
30 including orographic uplifting over the Hengduan Mountains, assisting frontal lifting in
31 the North China Plain, and facilitating convection in the Sichuan basin. In particular,
32 topography-induced leeside troughs over Indochina lead to strong convection that
33 assisted CO uplifting to the upper troposphere. This study shows that the new daytime
34 MOPITT near-infrared (NIR) and thermal-infrared (TIR) data (version 5 or above) have
35 enhanced vertical sensitivity in the free troposphere and may help qualitative diagnosis of
36 vertical transport processes in East Asia.

37

38 **1 Introduction**

39 Carbon monoxide (CO) plays several important roles in the atmosphere. The
40 oxidizing capability, an ability of the atmosphere to cleanse itself, is strongly influenced
41 by the CO level in the troposphere. CO near the surface is a major pollutant. Under high
42 NO_x conditions, CO is a precursor of ozone, while in low NO_x airmasses, CO helps ozone
43 destruction (Jacob, 1999; Holloway et al., 2000). As carbon dioxide (CO₂) is produced in
44 both ozone production and destruction processes (Holloway et al., 2000), CO is linked to
45 the global carbon cycle (Suntharalingam et al., 2004; Yurganov et al., 2008; Nassar et al.,
46 2010) affecting climate change. With a lifetime of weeks to months, CO is a good tracer

47 tracking transport of pollution. In the purview of these roles, it is important to understand
48 processes influencing the CO distribution and variability in the atmosphere.

49 Although the main sources of atmospheric CO and its mean status are generally
50 understood (Novelli et al., 1998; Jacob, 1999; Holloway et al., 2000), many processes
51 influencing CO variations at different time scales are not well known. Uplifting CO from
52 the boundary layer to the free troposphere (FT) is such a process, which usually occurs on
53 the synoptic scale that spans hundreds to thousands of kilometers in space and lasts hours
54 to days in time (Daley, 1991). Uplifted CO usually has a longer lifetime and can be
55 transported fast by the upper layer winds over long distances through continents and
56 between hemispheres in the troposphere (Stohl, 2001; Stohl et al., 2002; Damoah et al.,
57 2004). Uplifting air mass from the surface to FT generally takes place by three processes
58 (1) frontal lifting, (2) orographic lifting, and (3) deep convection (Brown et al., 1984;
59 Banic et al., 1986; Dickerson et al., 1987; Bethan et al., 1998; Pickering et al., 1998;
60 Chung et al., 1999; Donnell et al., 2001; Kowol-Santen et al., 2001; Cooper et al., 2002;
61 Liu et al., 2003; Miyazaki et al., 2003; Chan et al., 2004; Mari et al., 2004; Li et al., 2005;
62 Liu et al., 2006; Kar et al., 2008; Zhao et al., 2008; Ding et al., 2009; Randel et al., 2010;
63 Chen et al., 2012).

64 East Asia has experienced rapid development with increasing CO emission in the
65 past decades (Duncan et al., 2007). In addition to impacts on local air quality (Wang et al.,
66 2010), continuing increase in CO emissions will lead to great impacts on regional air
67 quality (Jaffe et al., 1999; Bertsch et al., 2004) and climate (Berntsen et al., 1999) of the
68 world because of an expected upward trend in pollution outflow from the region. East
69 Asia is characterized by its unique and complex meteorology, topography, and land

70 covers. Vertical transport of CO can be modulated by one or more of these conditions or
71 by their interactions. For example, the likelihood of when and where extratropical
72 cyclones are active is closely linked to the locations and frequency of frontal uplifting.
73 Wet and dry convections prevail in different seasons in northern China because of the
74 distinct climatological pattern in precipitation there (Dickerson et al., 2007). The
75 topography there also plays an important role in uplifting of CO alone and/or interplaying
76 with frontal systems, aiding convection in mountainous regions (Liu et al., 2003; Ding et
77 al. 2009). Recently, Lin et al. (2009) proposed a new mechanism that emphasizes the
78 impact of topography-induced leeside troughs over Indochina on strong convection. A
79 variety of land cover types in East Asia make CO sources there diversified. In highly
80 populated urban areas, such as those in the North China Plain, anthropogenic emissions
81 are high. Large biomass burning, occurring in areas with abundant vegetation, can
82 generate great amounts of CO for vertical transport when meteorological conditions
83 become favorable. Two such areas are Southeast Asia and the boreal forested area in
84 Russia (Wotawa et al., 2001; Schultz, 2002; Duncan et al., 2003). So far, our
85 understanding of the impacts of these processes and their interactions on CO uplifting is
86 still rather limited (Dickerson et al., 2007). The objectives of studying vertical transport
87 of CO in East Asia are to better understand the vertical distribution of CO in the region,
88 to advance the assessment of impacts of long-range transport of Asian CO on regions
89 downwind, and to help improve simulating this process in atmospheric models on the
90 synoptic scale, eventually leading to more realistic chemical weather forecast in the
91 future (Lawrence et al., 2003).

92 Due to lack of continuous measurements, most studies on CO in East Asia are based

93 on observations from periodic field campaigns (Jacob et al., 2003; Tsutsumi et al., 2003;
94 Li et al., 2007; Ding et al., 2009) or simulations by chemical transport models (Berntsen
95 et al., 1999; Bey et al., 2001) or both (Liu et al., 2003). CO measurements from satellites
96 provide unprecedented data revealing CO variations over East Asia. One of the
97 instruments is the Measurements Of Pollution In The Troposphere (MOPITT)
98 (Drummond, 1992; Drummond and Mond, 1996). MOPITT provides data of CO total
99 column and CO vertical profiles at several altitude levels, which are retrieved using a
100 nonlinear optimal estimation method theoretically based on the observed radiances and
101 their weighting functions, the a priori information, and the retrieval averaging kernels
102 (Rogers, 2000; Deeter et al., 2003). As a result, the MOPITT retrieval at one level can be
103 influenced by CO at other levels and thus MOPITT vertical resolution is coarse, generally
104 having only 2-3 pieces of independent information vertically in the troposphere.
105 MOPITT's vertical sensitivity was an issue in earlier applications of MOPITT data (Jacob
106 et al., 2003). Nevertheless, a few studies (Deeter et al., 2004; Kar et al., 2004, 2006, 2008;
107 Liu et al., 2006) demonstrated MOPITT's vertical sensitivity to some extent. Kar et al.
108 (2004) found Asian summer monsoon plumes in MOPITT CO data as a strong
109 enhancement of CO in the upper troposphere over India and southern China. Deeter et al.
110 (2004) illustrated similar distributions of the rain rate and the ratio of MOPITT CO at 350
111 hPa to at 850 hPa in the Tropical Eastern Pacific Ocean. Liu et al. (2006) observed large
112 differences (20-40 ppbv) in MOPITT CO at 250 hPa between two cases of vertical
113 transport of CO and attributed the differences to the respective weather systems.
114 Furthermore, the MOPITT data in new versions that use both thermal infrared and near
115 infrared radiances have offered enhanced vertical sensitivity (Worden et al., 2010; Deeter

116 et al., 2012; 2013). Therefore, a detailed examination of MOPITT's vertical sensitivity in
117 East Asia, especially for its ability in detecting vertical transport of high CO episodes, is
118 desirable.

119 In this study, three cases of high CO episodes in East Asia from 2003 to 2005 are
120 examined with MOPITT satellite data, in combination with aircraft measurements from
121 the Measurement of Ozone and Water Vapor by Airbus In-Service Aircraft (MOZAIC)
122 program (Marengo et al.,1998) (see Sects.2 and 4). The vertical transport mechanisms are
123 analyzed with simulations from a trajectory dispersion model FLEXPART (Stohl et al.,
124 2005) and a chemical transport model GEOS-Chem (Bey et al.,2001), along with other
125 meteorology data and satellite fire data (see Sects.2 and 4). MOPITT data are analyzed in
126 two ways. First, the vertical sensitivity of MOPITT is evaluated with the coincident
127 MOZAIC data (see Sect.3) and further illustrated with the three high CO episodes in
128 comparison with the MOZAIC data (see Sect.4). Second, the vertical variation in CO
129 captured by MOPITT is used to diagnose vertical transport of CO (see Sect. 4).
130 Discussion on the three cases is synthesized in Sect.5 and the major conclusions are
131 provided in Sect.6.

132

133 **2 Model and data**

134 **2.1 Satellite MOPITT CO data**

135 MOPITT is the first space instrument that targets continuous measurements of
136 tropospheric CO. MOPITT has been onboard of the Terra satellite launched in 1999,
137 making scientific measurements since March 2000.Terra is flying in a sun synchronous
138 polar orbit with an altitude of 705 km, crossing the equator at ~10:45 and 22:45 LT and

139 making 14-15 daytime and nighttime overpasses each day. MOPITT uses a cross-track
140 scanning method with a swath of 29 pixels (4 pixels in a row), each pixel being 22 km ×
141 22 km. Therefore, with a swath of ~600 km, only about one third of the global area is
142 covered in a day. Additionally, clouds can cause even more gaps in MOPITT daily data.
143 This makes it challenging to use MOPITT data for synoptic studies. It takes 3 days to
144 achieve a near-complete global coverage (Edwards et al., 1999) if assuming no blocks
145 from clouds.

146 MOPITT measures upwelling radiation in two narrow infrared spectral regions for
147 CO retrieval: (1) a thermal-infrared (TIR) band near 4.7 μm that has strong carbon
148 monoxide absorption and (2) a near-infrared (NIR) band near 2.3 μm that has weak CO
149 absorption. MOPITT Version 5 retrieval products are significantly different from earlier
150 products and offer three distinct products depending on application requirements. One of
151 them is a TIR/NIR “multispectral” product, which has enhanced sensitivity to CO in the
152 lower-most troposphere (Worden et al., 2010; Deeter et al., 2012; 2013). Validations and
153 evaluations of MOPITT data in various versions are documented in Emmons et al. (2004),
154 Worden et al. (2010), and Deeter et al. (2012, 2013).

155 We first examined the MOPITT vertical sensitivity through comparison between
156 coincident MOPITT and MOZAIC CO profiles. Advances of Version 5 (V5, a TIR/NIR
157 “multispectral” product) from Version 4 (V4, a TIR-only product) data were assessed
158 with the level 2 data. Then, V5 level 2 data were used throughout the case studies, in
159 which MOPITT data were gridded horizontally into 0.25 °latitude × 0.25 °longitude and
160 at the MOPITT vertical resolution of 100 hPa from the surface to 100 hPa.

161

162 **2.2 Aircraft MOZAIC CO data**

163 The Measurement of Ozone and Water Vapor by Airbus In-Service Aircraft
 164 (MOZAIC) program was initiated in 1993 by European scientists, aircraft manufacturers,
 165 and airlines to collect experimental data (Marenco et al., 1998). MOZAIC consists of
 166 automatic and regular measurements of ozone, CO, and water vapor by several long
 167 range passenger airliners flying all over the world. The aim is to build a large database of
 168 measurements to allow studies of chemical and physical processes in the atmosphere.

169 In comparing MOPITT with MOZAIC CO data, coincident MOPITT and MOZAIC
 170 data from 2003 to 2005 were screened within a radius of 1.5 ° and within a 4 h period.
 171 The radius of 1.5 ° was applied to selected MOZAIC profiles at 500 hPa and the
 172 MOZAIC slant path was included in the radius. MOZAIC profile was smoothed by
 173 applying the MOPITT averaging kernels and the a priori profile for the co-located
 174 retrieved MOPITT profile to account for the bias introduced by the averaging kernels and
 175 the a priori. Therefore, the smoothed MOZAIC CO profile $\hat{\mathbf{x}}^{MOZAIC}$ is derived by
 176 (Rogers, 2000)

177
$$\hat{\mathbf{x}}^{MOZAIC} = \mathbf{x}_a^{MOPITT} + \mathbf{A} (\mathbf{x}^{MOZAIC} - \mathbf{x}_a^{MOPITT}) \quad (1)$$

178 where $\mathbf{A} = \partial \hat{\mathbf{x}} / \partial \mathbf{x}$ is the MOPITT averaging kernel matrix which describes the sensitivity
 179 of the MOPITT CO estimate to the true profile of CO, \mathbf{x}^{MOZAIC} is the MOZAIC CO
 180 profile, which has been mapped to the MOPITT pressure grid. The quantity \mathbf{x}_a^{MOPITT} is
 181 the MOPITT a priori, which is based on CO simulations from the MOZART model
 182 (Emmons et al., 2004).

183 The MOZAIC measurements usually extend from the surface to ~ 250 hPa.
 184 When validating MOPITT data using Eq.(1), CO mixing ratios above 300 hPa was

185 supplemented with CO from the GEOS-Chem chemical transport model (see Sect.2.6) on
186 the same location and day, similar to the treatments by Worden et al.(2010), who used the
187 MOZART climatology simulations. Because CO above 250 hPa is lower than that in the
188 middle and lower troposphere, the bias due to this treatment is expected to be low.

189

190 **2.3 MODIS fire count data**

191 The Moderate-resolution Imaging Spectroradiometer (MODIS) is a type of
192 instruments which have been onboard of the Terra (EOS AM) satellite since 1999 and on
193 the Aqua (EOS PM) satellite since 2002. The MODIS fire products include a validated
194 daily global active fire product (MOD14 Terra and MYD14 Aqua) (Justice et al., 2002),
195 generated using a global active fire detection algorithm that uses a multispectral
196 contextual approach to exploit the strong emission of midinfrared radiation from fires
197 allowing subpixel fire detection (Giglio et al., 2003). The horizontal resolution is 1 km.
198 The fire data are acquired from the Fire Information for Resource Management System
199 (FIRMS) (Davies et al., 2009).

200

201 **2.4 NCEP FNL meteorological data**

202

203 The NCEP Final (FNL) global tropospheric analyses are on 1 °by 1 °grids every 6h
204 (<http://rda.ucar.edu/datasets/ds083.2/>). Parameters in FNL include surface pressure, sea
205 level pressure, geopotential height, temperature, sea surface temperature, potential
206 temperature, relative humidity, precipitable water, u and v winds, and vertical motion,
207 available on the surface, at 26 levels from 1000 to 10 hPa, the tropopause, the boundary
208 layer, and a few others. In addition to driving FLEXPART (see Sect. 2.5), the FNL data

209 are used to analyze the meteorological conditions including the surface pressure, wind
210 fields, and development of a cyclone. The data are generated from the Global Data
211 Assimilation System (GDAS).

212

213 **2.5 The FLEXPART trajectory model**

214 To diagnose the transport processes and trace CO sources, we used the FLEXPART
215 model (Stohl et al., 2005), which is a Lagrangian Particle Dispersion Model developed at
216 the Norwegian Institute for Air Research in the Department of Atmospheric and Climate
217 Research. FLEXPART can be driven by meteorological input data generated from a
218 variety of global and regional models. In this study, the simulations were driven by the
219 NCEP FNL data. This model has been extensively validated (Stohl et al., 1998;
220 Cristofanelli et al., 2003) and widely used in studies of the influence of various
221 meteorological processes on pollution transport (Cooper et al., 2004, 2005, 2006;
222 Hocking et al., 2007; Ding et al., 2009; Barret et al., 2011; He et al., 2011; Chen et al.,
223 2012). In running FLEXPART, a large number of particles are released from defined
224 locations (latitude, longitude, and altitude) at a time. Backward or forward trajectories of
225 the particles are recorded in latitude (°), longitude (°), and altitude (km) every hour.

226

227 **2.6 The GEOS-Chem chemical transport model**

228 GEOS-Chem is a global three dimensional chemical transport model
229 (<http://geos-chem.org>). The model contains detailed description of tropospheric
230 O₃-NO_x-hydrocarbon chemistry, including the radiative and heterogeneous effects of
231 aerosols. It is driven by assimilated meteorological observations from the National

232 Aeronautics and Space Administration (NASA) Goddard Earth Observing System
233 (GEOS) from the Global Modeling and Assimilation Office (GMAO). In this study,
234 GEOS-Chem version v9-1-3 was employed and executed in the full chemistry mode,
235 which is driven by GEOS meteorology with temporal resolution of 6h (3h for surface
236 meteorological variables), with a horizontal resolution of 2 °latitude by 2.5 °longitude
237 and 47 vertical levels, including ~35 levels in the troposphere from 1000 to 100 hPa.

238 GEOS-Chem uses anthropogenic emissions from the Emissions Database
239 for Global Atmospheric Research (EDGAR) global inventory (Olivier and Berdowski,
240 2001), which are updated with regional inventories, including the emission inventory in
241 Asia (Streets et al., 2006; Zhang et al., 2009). The biomass burning emissions are from
242 the Global Fire Emissions Data (GFEDv3) monthly inventories (van der Werf et al., 2010)
243 and biogenic VOC emissions are taken from the Model of Emissions of Gases and
244 Aerosols from Nature (MEGAN) global inventory. Emissions from other natural sources
245 (e.g., lightning, volcanoes) are also included.

246 The model has been extensively evaluated and used in studies of atmospheric
247 chemistry and pollution transport (Bey et al., 2001; Heald et al., 2003; Liu et al., 2003;
248 Liu et al., 2006; Zhang et al., 2006; Jones et al., 2009; Nassar et al., 2009; Kopacz et al.,
249 2010; Jiang et al., 2011). GEOS-Chem can generally describe CO variability in the
250 troposphere but somewhat underestimate the observations in the northern mid-latitudes
251 possibly due to biases in the CO inventory or numerical diffusion in the model or both
252 (Heald et al., 2003; Duncan et al., 2007; Nassar et al., 2009; Kopacz et al., 2010).

253

254 **3 Comparison between MOPITT and MOZAIC CO profiles**

255 MOPITT's vertical sensitivity can be described in terms of the averaging kernels
256 (see Eq.1) and the Degree of Freedom for Signal (DFS). The averaging kernel matrix
257 indicates the sensitivity of the MOPITT CO estimate to the true CO profile, with I
258 (identity matrix) being the best, when true CO profiles are retrieved, and 0 being the
259 worst, when MOPITT retrievals just take the a priori. In reality, the average kernel matrix
260 is less than I, implying some contribution of CO from other levels to the retrieved level so
261 that the CO vertical structure cannot be fully resolved. DFS gives the number of
262 independent pieces of information available vertically in the measurements and it is the
263 sum of the diagonal elements of the averaging kernel matrix (Rogers, 2000). Figure 1
264 shows a yearly mean of DFS for daytime and nighttime, respectively, in East Asia for the
265 V5 TIR/NIR data, indicating substantial increases in DFS compared to earlier MOPITT
266 versions (Worden et al., 2010; Deeter et al., 2012). The daytime DFS in East Asia (Fig.1a)
267 ranges from 0.5 to 2.7, usually decreasing with latitude, similar to its distribution in other
268 regions and on the global scale (Deeter et al., 2004; Worden et al., 2010). In the same
269 latitudinal zones, the DFS is higher over land than over ocean. The daytime annual DFS
270 is high in the Sichuan basin, the eastern part of mainland China, the Indochina peninsula,
271 and the Indian subcontinent. Over the mountain or valley regions, DFS is low, such as
272 above the Tibetan Plateau. The stars indicate the cities where MOZAIC vertical
273 measurements are available for validation of MOPITT data. The annual mean DFS is
274 1.65, 1.51, 1.60, and 1.64, respectively, in an area of $1^\circ \times 1^\circ$ around Beijing, Narita,
275 Shanghai, and Hong Kong, with a maximum of 1.98, 1.64, 1.81, and 1.74 for the cities,
276 respectively. The nighttime DFS values (Fig. 1b) are lower (from 0.5 to 1.5) than the
277 daytime values, similar to that in Deeter et al. (2004) for an earlier MOPITT version.

278 Spatially, nighttime DFS is high over regions where the daytime DFS is also high.

279 The general patterns of MOPITT averaging kernels have been documented (Pan et
280 al., 1998; Emmons et al., 2004; Deeter et al., 2003, 2004, 2012; Kar et al., 2008; Worden
281 et al., 2010). For V5 MOPITT data, the averaging kernels at the four cities are similar to
282 these in Worden et al. (2010, in their Fig. 7). The difference in the averaging kernels
283 between V4 and V5 can be as large as 0.14 in the surface and lower troposphere and as
284 0.10 in the upper troposphere (not shown).

285 Figure 2 shows the relative bias between MOPITT and the smoothed MOZAIC
286 ($\hat{\mathbf{x}}^{MOZAIC}$) profiles (see Eq. 1), which is also referred as “MOPITT estimate of in situ” in
287 Worden et al. (2010) and “transferred profile” in Emmons et al. (2004). For V5 data (in
288 red), the mean bias is within $\pm 20\%$ for all the cities. In all the altitude levels, the bias is
289 smallest (close to zero) around 500-400 hPa and increases upward and downward. The
290 bias is mostly positive above 500-400 hPa, while below 500-400 hPa, it is positive at
291 Beijing, Narita but negative at Shanghai and Hong Kong. Whether the sign change is
292 related to the change in the geographic location (Shanghai and Hong Kong are both coast
293 cities) can be a subject for further study. The V4 data (in green) also show the smallest
294 bias in the middle troposphere. In the lower troposphere, the bias in V5 is reduced by
295 5-10% at Beijing and Narita. At Shanghai and Hong Kong, the bias changes from
296 positive in V4 to negative in V5, with a smaller (at Shanghai) or larger (at Hong Kong)
297 magnitude. In the upper troposphere above 500-400 hPa, the bias in V5 at Beijing, Narita,
298 and Shanghai changes to positive, with a magnitude as the same as or larger than in that
299 in V4. At Hong Kong, the bias in V5 remains positive but the magnitude is enlarged.
300 Deeter et al. (2013) compared MOPITT data with the NOAA aircraft measurements over

301 North America and data from the HIAPER Pole to Pole Observations (HIPPO) field
302 campaign data (Wofsy et al., 2011). They found a positive bias in MOPITT V5 TIR/NIR
303 data at 400 hPa (4%) and 200 hPa (14%). They also showed a latitude-dependent positive
304 bias in the northern hemispherical upper troposphere in MOPITT V3 and V4 data. This
305 study suggests an overall positive bias, agreeing with Deeter et al. (2013) in magnitude
306 and sign, in MOPITT V5 data for the upper troposphere. As a comparison, we also
307 validated MOPITT data in other cities in the globe and found that the mean bias in
308 Europe or the United States is lower than in East Asia, especially in the surface layer (not
309 shown).

310 The correlation between MOPITT and smoothed MOZAIC data is shown in Fig. 3.
311 From 500 to 100 hPa, the correlation coefficient between the two data sets is 0.92, 0.86,
312 0.83, 0.68 at Beijing, Narita, Shanghai, and Hong Kong, respectively (Fig.3a), while from
313 the surface to 600 hPa, the correlation becomes closer, being 0.90,0.92, 0.92, 0.94 at
314 Beijing, Narita, Shanghai, and Hong Kong, respectively (Fig. 3b). The correlation
315 coefficient between the two data is the best in the middle troposphere (500-400 hPa, not
316 shown).

317

318 **4 Uplifting of CO to the free troposphere**

319 Daily MOPITT and MOZAIC data from 2003-2005 were screened to find cases of
320 high CO episodes observed by both MOPITT and MOZAIC at the same location and
321 time. We found three cases of high CO in MOPITT data with close-by MOZAIC
322 measurements, while it was hard to find such high CO episodes with exact coincident
323 MOPITT and MOZAIC observations because of large gaps in MOPITT data and limited

324 aircraft sampling coverages. In the three cases, high CO concentrations up to 300-500
325 ppbv are observed by MOZAIC in the free troposphere from 750 to 350 hPa.

326 In the following, we provide detailed analyses of each case, ordered by year of
327 occurrence in Table 1. The cases occurred over the East China Sea or the Sea of Japan or
328 both. High CO was shown in MOPITT daytime data in the middle to upper troposphere
329 in case 2003, mostly in the lower to middle troposphere in case 2004, and in the upper
330 troposphere in case 2005. For comparison, MOPITT and MOZAIC observations for the
331 three cases are shown in Figs. 4-6, followed by analyses for each case with FLEXPART
332 and GEOS-Chem simulations, in combination with MODIS fire data and NCEP FNL
333 meteorological data. Table 1 provides a brief summary for all the cases. The cases
334 occurred in spring and summer when cyclone activities are strong in East Asia (Chen et
335 al., 1991; Yue and Wang, 2008). The CO sources are identified as biomass burning or a
336 combination of biomass burning and anthropogenic origins. The outflow of the high CO
337 episodes finally reached the boundary layer at the west coast of the United States and
338 Canada.

339

340 **4.1 Case study I: 6 June 2003**

341 On 6 June 2003, a large area ($\sim 400 \text{ km} \times 1500 \text{ km}$) of high CO up to 350 ppbv
342 appeared in the MOPITT image over the Sea of Japan and the nearby continent in the
343 middle to high troposphere (Fig. 4a). In Fig. 5a, the MOPITT CO profile averaged over
344 the boxed area in Fig. 4a shows a broad enhancement from the monthly profile between
345 650-300 hPa, with peak CO abundances of ~ 300 ppbv appearing around 550 hPa. The
346 large difference between the MOPITT a priori and the measurements over these altitudes

347 indicates MOPITT's capability of capturing pollution episodes with some degree of
348 vertical sensitivity. The vertical sensitivity is demonstrated through (1) the strongest CO
349 source among the three cases was captured by the largest magnitude of CO enhancement
350 of 200-250 ppbv from the a priori, (2) the altitude of the maximum CO enhancement was
351 detected around the middle troposphere, in contrast to the other two cases which show the
352 maximum in the lower-middle and upper troposphere, respectively, and (3) the elevated
353 CO was over a broad range of altitudes as the vertical resolution of MOPITT is rather
354 coarse, i.e., the maximum DFS is about 2.5 (Figure 1). This CO peak was not shown in
355 the MOPITT monthly mean profile, reflecting the episodic nature of this event. The high
356 CO episode was also captured by a near-by MOZAIC measurement (Fig. 5b). A layer of
357 elevated CO is apparent between 500-350 hPa, with a CO peak up to ~ 550 ppbv around
358 400 hPa. In addition, the MOZAIC relative humidity (RH) and ozone profiles are shown
359 in Fig. 5b. Around the altitudes of CO buildup, elevated humidity followed the CO
360 profile, while ozone also showed some enhancement.

361 A latitude-altitude cross section from MOPITT is shown in Fig. 6a. It is the average
362 between two blue dashed lines in Fig. 4a. The arrows represent the winds in the
363 meridional and vertical directions and the contour represents the zonal wind speed.
364 Consistent with Fig. 4a, high CO up to 350 ppbv appears in the middle to upper
365 troposphere between 35-50 °N.

366 To trace down the CO source, backward trajectories of the air particles were
367 simulated using FLEXPART after releasing 30 000 and 7000 particles, respectively, from
368 the locations of the large and small boxed areas in Fig. 6a (the same as the blue bars in
369 Fig. 4a) on 6 June 2003 when CO was high in the MOPITT data. Because CO has a

370 relatively long lifetime (weeks to month), it is assumed that CO is not removed in the
371 backward trajectories. Figure 7 shows the distribution of particle concentration between
372 6.25-10.25 km (~ 500-250 hPa, Fig. 7a) and between 0-3.25 km (~ 1000-650 hPa, Fig. 7b).
373 The contour lines indicate the geopotential height at 850 hPa at 12:00 UTC on 3 June
374 2003 (Fig. 7a) and at 0 UTC on 2 June 2003 (Fig. 7b), respectively. The stars, diamonds,
375 and circles in Fig. 7b show the location of large forest fires near Lake Baikal from
376 MODIS fire data. The circles, diamonds, and stars denote daily mean fire counts of
377 20-100, 100-300, and 300-500 per $2.5 \times 2.5^\circ$ grid area, respectively, from 31 May to 6
378 June. The high particle counts between 0-3 km in the vicinity of Lake Baikal match well
379 with the location of fire counts (Fig. 7b). On 3 June 2003, there was a cyclone with a cold
380 frontal system (Fig. 7a) that rapidly lifted the CO originated from the fires along the
381 warm conveyor belt (WCB) to the upper level. The particle distribution in the upper
382 troposphere shows the transport pathway of the particles to the Sea of Japan. To further
383 illustrate this, particles were released from the fire region near Lake Baikal ($93-115^\circ\text{E}$,
384 $50-60^\circ\text{N}$, 0-3 km, following Lavoué et al. (2000), who found an average injection height
385 of Siberian fires of ~ 3 km). Forward trajectories were simulated and the resultant vertical
386 distribution of the particles varying with time during 1-15 June 2003 is shown in Fig. 8. It
387 is found that the released particles from the fires traveled along the isobars to northeast of
388 Lake Baikal from 1 June to 3 June 2003 and then the particles were lifted to the upper
389 layers (3-8 km) on 3 June at 12 a.m. (in 60-70 h) (Fig. 8). Then, the particles were
390 transported to the east along these altitudes. On 6 June (in 120-140 h), a large amount of
391 particles appeared in a layer of 3-8 km (Figs. 8 and 4a). The altitudes with high particle
392 concentrations agree well the MOPITT data between 650-350 hPa (Figs. 4a and 6a).

393 It is the cyclone with a front northeast of Lake Baikal that transported the CO up
394 along the WCB (Figs. 7a and 8). Figure 5b shows that the relative humidity reached about
395 65 % in MOZAIC measurement, suggesting the air mass indeed came from a WCB
396 (Cooper et al., 2002). The MOZAIC ozone profile also shows elevated ozone at the same
397 altitudes but the shape does not follow exactly the ones of CO and humidity, implying
398 complexity of chemical processes involved. The polluted air reached as high as 9 km
399 although most particles remained at heights of about 3-8 km (Fig. 8). After being lifted to
400 higher altitudes, the polluted air was transported by strong westerlies over long distances.
401 Figure 8 shows that the particles were further transported to the east and sink slowly after
402 7 June. Around 14 June 2003, the particles reached the east coast of Canada (0-5 km).
403 The satellite MODIS data show a large number of hot spots near Lake Baikal in May and
404 June 2003. Earlier studies have shown that forest fires in Asia can impact air quality in
405 North America (Jaffe et al., 2004; Liang et al., 2004; Oltmans et al., 2010). This case
406 illustrates again the role that WCBs played in the intercontinental transport of pollution
407 for such high CO. It should be noted that the FLEXPART simulation was made by using
408 the FNL meteorological data, which may have not considered the buoyancy force due to
409 fires. Such buoyancy force can lift CO plumes even faster and higher.

410 Our analyses are consistent with Nédec et al. (2005), who analyzed 320 MOZAIC
411 flight routes from Europe to Asia in 2003 and reported the observations of high CO up to
412 800 ppbv above 8 km (~ 350 hPa) on 3 and 4 June 2003 around 57 °N (northeast of Lake
413 Baikal). This matches well with the time and location of frontal lifting of CO in this
414 FLEXPART simulation. With analyses of different data sets, i.e., Along Track Scanning
415 Radiometer (ATSR) fire data, the Total Ozone Mapping Spectrometer (TOMS) aerosols

416 data and the MODIS cloud data, Nédec et al. (2005) also attribute the high CO at these
417 altitudes to front lifting of CO from large forest fires near Lake Baikal. Furthermore, this
418 analysis provides a detailed description on the CO transport pathways (Figs. 7 and 8). We
419 found that this case, caused by the strongest CO source among the three cases, show the
420 largest horizontal area with CO plumes (Fig. 5), the widest vertical CO buildup with
421 strongest abundances (Fig. 7), and the biggest enhancement of 200-250 ppbv from the a
422 priori (Fig. 6).

423

424 **4.2 Case study II: 18 March 2004**

425 This case occurred on 18 March 2004 when high CO appeared in the MOPITT data
426 in the lower and middle troposphere over the East China Sea (Fig. 4b). The elevated CO
427 of 200-250 ppbv is observed between 750 and 550 hPa vertically in MOPITT data (Fig.
428 5c). The departure of the MOPITT CO profile from its a priori reflects the MOPITT's
429 vertical sensitivity (Fig. 5c). The MOPITT monthly mean, like for the other two cases,
430 follows a typical CO profile pattern with CO concentrations being the highest near the
431 surface and decreasing gradually with altitude. The CO on 18 March 2004 was 50 ppbv
432 higher than the monthly mean above 800 hPa. A layer of large elevated CO appeared in
433 the MOZAIC profile between 750-550 hPa with a peak of 500 ppbv around
434 650 hPa (Fig. 5d). The high RH (~ 90-100 %) below 600 hPa in the MOZAIC data
435 suggests that the air mass experienced some uplifting process that enhanced its humidity,
436 likely from a WCB. The MOZAIC ozone peaked (~ 70 ppbv) around the same altitudes
437 as CO, implying that ozone may be produced in the air mass carrying high CO during the
438 transport process. Figure 6b shows a latitude-altitude cross section averaged between the

439 two blue dashed lines in Fig. 4b. Around 30 °N, elevated CO levels (~ 200 ppbv) are
440 evident around 700 hPa. The corresponding winds (blue lines and arrows) show that there
441 were strong descents north of the elevated CO and moderate ascents in the south of the
442 region (Fig. 6b), indicating the formation of a frontal system with downward and upward
443 flows, south and north of the front, respectively.

444 This case was simulated with GEOS-Chem to identify the sources of CO and to
445 explore the transport mechanisms. The MODIS fire data suggest biomass burning over
446 northern Indochina peninsula to be a source for the observed high CO (Fig. 9). The time
447 series of fire counts over area of 20-25 °N and 92-105 °E peaked on 12 March 2004.
448 Correspondingly, high CO of ~ 300 ppbv appeared in the MOPITT composite of 11-18
449 March 2004 at 700 hPa over northern Indochina peninsula (Fig. 9). In the GEOS-Chem
450 simulation (Fig. 10b), this source is also recognized. In addition, the anthropogenic
451 source concentrated over the North China Plain (NCP) (approximately 30-40 °N, 110-125 °
452 E) is identified as another source of high CO (Fig. 10c). Figure 11 shows the
453 latitude-altitude cross sections of the GEOS-Chem simulations of CO, fire-induced CO,
454 and anthropogenic CO, respectively, along 130 °E on 18 March 2004. The CO from
455 biomass burning was more widely spread to the south than the anthropogenic CO. CO
456 abundances from both sources were high around 700 hPa (Fig. 11b and c) between 25-35 °
457 N across 130 °E where MOPITT observed high CO (Fig. 6b).

458 The different CO distributions for the two sources in three dimensions (Figs. 10 and
459 11) reflect rather different transport pathways and uplifting mechanisms. The transport of
460 the fire-induced CO can be divided into the following four processes. First, the CO was
461 orographically lifted along the Hengduan Mountains from the surface to ~ 750 hPa. The

462 lifted CO is shown in Fig. 12 around 100 °E on a longitude-altitude cross section along
463 22 °N. Then, the CO experienced two separate transport pathways. In the second process,
464 part of the lifted CO was further transported upward to 400-300 hPa, shown as a bulb in
465 Fig. 12 around 105 °E. This is due to strong convection, possibly caused by a frontal
466 system developed on March 17, 2004 (Fig. 9), interplayed with the leeside troughs east of
467 the Hengduan Mountains. The vertical velocity reached 0.2 m s^{-1} in FNL data around this
468 level (not shown). The ECMWF (European Centre for Medium-Range Weather Forecasts)
469 data also show northeastward airflow from Indochina peninsula with high potential
470 energy (warm and wet) available for strong convection. All of these suggest that the
471 strong convection over the leeside troughs rapidly lifted CO up to ~350 hPa. In fact, the
472 orographic lifting and topography-induced convection are quite common in this region so
473 high CO often appears at these two altitudinal levels in March as simulated by
474 GEOS-Chem (not shown). On 17 March, the lifted CO was with even higher
475 concentrations (~ 500 ppbv) around 400 hPa than the monthly mean because of the high
476 CO source from large forest fires. In the third process, the uplifted CO around 400-300
477 hPa (near 105 °E in Fig. 12) was transported northeastward by strong winds along the
478 front in the upper troposphere, reaching the East China Sea (near 30 °N, 130 °E) on 18
479 March (Figs. 10b and 11b). This transport enables high CO from forest fires in southern
480 Asia in low latitudes to rapidly reach the upper troposphere in the mid-latitudes. In the
481 fourth process, paralleling to the second and third, part of the orographically lifted CO
482 stayed around ~700 hPa because of leeside-trough induced convection. This CO was
483 transported eastward along the isobars of the low pressure system around 700 hPa (Figs.
484 10 and 12). This process occurred at lower altitudes than processes two and three. The

485 transport was slower and it took longer time (from 15 to 18 March) for the CO to reach
486 the East China Sea. Processes two and three brought CO to the upper troposphere, while
487 process four increased CO in the lower to middle troposphere (Fig. 11b). For the
488 anthropogenic CO in the North China Plain, the vertical transport was mainly carried out
489 by frontal lifting. Horizontally, anthropogenic CO was transported eastward along 30 °N
490 (Fig. 10c). Consequently, the total CO shows a buildup centered near 700 hPa around 30 °
491 N and 130 °E, mostly coming from the two CO sources (Fig. 11a-c).

492 The Hengduan Mountains run mainly north to south, with elevations ranging from
493 1300 to 6000 metres. This topography provides a favorable condition for the formation of
494 the leeside troughs if meteorology is satisfied. Such troughs promote vertical transport of
495 CO on the west flank of the Mountain (in the second and fourth processes), while the
496 orographic lifting occurred on the east flank of the Mountains (in the first process).

497 Comparison of the simulated vertical structure of CO (Fig. 11a) with the MOPITT
498 observation (Fig. 6b) shows that MOPITT can generally capture vertical transport of CO
499 from forest fires and anthropogenic sources, although the magnitude of CO in MOPITT
500 data was lower and there were also substantial gaps in the MOPITT images due to
501 convective clouds. In the MOPITT data, high CO of ~ 200 ppbv reached up to 200 hPa.
502 In the lower to middle troposphere, elevated CO (~ 200 ppbv) was centered around
503 650-700 hPa. These features are similar to the GEOS-Chem simulations. Note that the
504 CO buildup around 300 hPa in the GEOS-Chem simulation (Fig. 11a and b) was reflected
505 in the MOPITT data (Fig. 6b), but not as obvious as in the simulation since the MOPITT
506 retrievals are smoothed with the averaging kernels. This CO is also shown as a little
507 bump around 300 hPa in MOPITT vertical profile in Fig. 5c. This buildup is missing in

508 the MOZAIC profile (Fig. 5d) because the aircraft flew towards the north and outside the
509 region with high CO.

510 As the backward trajectories starting from the boxed area in Figure 4b indicated the
511 most particles came from the large fire regions starting from 11 March 2004, air particles
512 were released in FLEXPART over the regions from the surface to 1 km on 11 March
513 2004, and forward trajectories were simulated to track down the air parcels until 18 May
514 2004 at 2 a.m. Taking the same zonal means as for Fig. 6b, it is found that the vertical
515 distribution of particle concentrations is similar to that in Fig. 6b with highest particle
516 concentrations between 4-5 km (not show). As simulated by FLEXPART, the outflow of
517 the high CO finally reached the west coast of the United States with particles mainly
518 distributed around 5 km in altitude. High CO observed in East Asia in this case appeared
519 the most southerly among the three, leading to a most southerly outflow.

520 The transport mechanism of biomass burning by the fourth processes was first
521 proposed by Lin et al. (2009) who found that the leeside troughs above the Indochina
522 peninsula play a significant role in uplifting of ozone there as there is lack of tropical
523 deep convection to explain such strong convection. In this study, we even found these
524 leeside troughs promote vertical transport of CO to the upper troposphere (the second
525 process, Fig. 12). It is the interplay of the leeside troughs and the cyclone in the northeast
526 of China which formed a front system that transported CO from the Indochina peninsula
527 upward.

528

529 **4.3 Case study III: 10 April 2005**

530 In this case, MOPITT observed high CO of ~ 250 ppbv at 300 hPa near the east coast

531 of Japan on 10 April 2005 (Fig. 4c). To compare MOPITT and MOZAIC data, the mean
532 MOPITT profile was taken over a boxed area (in Fig. 4c) upwind of the MOZAIC
533 measurement. The MOPITT vertical profile clearly shows a CO peak around 300 hPa,
534 where it departs from the MOPITT monthly mean (Fig. 5e). Comparing with cases 2003
535 and 2004, MOPITT CO peaked at higher altitudes, illustrating some MOPITT vertical
536 sensitivity even at these altitudes. In Fig. 5f, a sharp peak of 300 ppbv in MOZAIC CO is
537 shown around 350 hPa. The profile of relative humidity follows closely that of CO, with
538 values up to 90-100 % around 350 hPa, implying that the elevated CO was lifted to this
539 level from the lower troposphere by a cyclone system along its WCB. However, the
540 MOZAIC ozone profile varies differently from the CO and relative humidity profiles.
541 This is found due to a strong stratospheric intrusion introduced by the cyclone. HYSPLIT
542 simulations suggest that a large amount of air mass plunged around 4 April from 9 to 3-4
543 km over northwest of China, bringing high ozone to the lower troposphere (not shown).
544 Miyazaki et al. (2003) also observed downwelling of stratospheric air on the back side of
545 cyclones. Figure 6c shows an altitude-latitude cross section averaged between 120-150 °E
546 (between two dashed lines in Fig. 4c). High CO of 200-250 ppbv appeared between
547 300-200 hPa around 35 °N. This is a rare case in which MOPITT reports such high CO
548 (200-250 ppbv) at these high altitudes (around 300 hPa). Documented CO abundances
549 observed by MOPITT at these altitudes were ~130 ppbv over Indian summer monsoon
550 seasons (Kar et al., 2004), 110-150 ppbv in the North America from the forest fires,
551 chemical, and anthropogenic sources (Liu et al., 2005; 2006), and ~150 ppbv in spring at
552 Hong Kong (Zhou et al., 2013).

553 The MODIS fire data show that there were indeed large fires over Indochina

554 peninsula in 3-10 April 2005, shown as stars in Fig. 13. Using GEOS-Chem, CO from
555 fire and anthropogenic sources was simulated to identify their respective contributions
556 and transport pathways.

557 The entire process of vertical transport of CO is well reproduced by GEOS-Chem
558 (Fig. 14). Figure 14a provides the CO distribution in the lower troposphere on 8 April
559 2005, while Figs. 14b and 14c show the CO distribution on the next day and the day after
560 in the middle and upper troposphere, respectively. The geopotential heights at 750, 450,
561 and 250 hPa are overlaid with the CO images for each layer accordingly. On 8 April 2005,
562 there was a cyclone developing in the east of Lake Baikal between 110-120 °E, 45-55 °N.
563 The surface CO was transported upward and northeastward along the WCB (Fig. 14a).
564 On 9 April, the cyclone moved to the east (Figs. 13 and 14b). The high CO shows a
565 “comma” shape along WCB at the mid-troposphere; this shape is typical for a mature
566 cyclone system with a WCB (Cooper et al., 2002). The cyclone further moved eastward
567 and reached the Sea of Japan on 10 April (Fig. 14c). The GEOS-Chem simulation shows
568 accumulation of high CO over the ridge of high pressure and along the front at the upper
569 troposphere. The GEOS-Chem simulations suggest that the outflow of the high CO
570 reached Canada on 16 April.

571 The combined effects of cyclone activities, topography, and CO from different
572 sources and locations are reflected in distinct CO signatures along the WCB. Figure 15
573 shows the CO from the fires (Figs. 15a and 15c) and from the anthropogenic source (Figs.
574 15b and 15d) in the middle and upper troposphere, respectively, overlaid with the
575 geopotential height at 450 hPa (Figs. 15a and 15b) and 250 hPa (Figs. 15c and 15d),
576 respectively. In the middle troposphere (500-400 hPa), a large amount of CO from the

577 fires in Indochina peninsula was uplifted to this level along the middle part of the WCB
578 on 9 April 2005 and was transported eastward on 10 April, 2005 (Fig. 15a). One source
579 of the anthropogenic CO was concentrated around the North China Plain (Ding et al.,
580 2009) where high CO was evident in MOPITT data (Fig. 13, 35-45 °N, 100-120 °E) (Fig.
581 15b). On 8 April, this CO was uplifted along the WCB and further transported to the
582 middle troposphere, coming across sudden elevated terrains on the way and forming the
583 head of the “comma” in the cyclone system (Figs. 14b and 15b). The topography's role
584 was noticed by Liu et al. (2003), who found a ring of convergence around the North
585 China Plain associated with elevated terrain, and by Ding et al. (2009), who speculated
586 possible topography lifting in North China Plain. In the southern end of the WCB (near
587 30 °N, 120 °E in Fig. 15b), the CO came from the anthropogenic source in the vicinity of
588 the Sichuan basin (~ 26-34 °N, 102-110 °E). This CO was transported vertically to 500
589 hPa on 8 April at 18:00 UTC to 9 April at 00:00 UTC. Air pollution often accumulates in
590 the Sichuan basin because of its special topography. The development of small scale
591 cyclones there is well known as the southwest vortex or Sichuan low (Tao and Ding,
592 1981). Accumulated pollutants there usually are transported to the free troposphere by
593 such convection. The strong convection can last more than 6 h and peak at the midnight
594 (Yu et al., 2007). As this anthropogenic source is quite stable, its contribution should not
595 be understated.

596 Interestingly, Lin et al. (2009) reported an observed ozone enhancement from
597 ozonesonde data at 4 km in Taiwan on 11 April 2005. They proposed a new transport
598 mechanism from their study as discussed in Sect. 4.2, in which they attributed the
599 elevated ozone to the biomass burning in Indochina. Similarly, CO from biomass burning

600 is also apparent over Taiwan at the middle troposphere in the GEOS-Chem simulation
601 (Fig. 15a), although the maximum CO enhancement was north of Taiwan at this altitude.

602 The white dot in Fig. 15 indicates the location where MOZAIC passed over. It is clear
603 that MOZAIC measurement was within the WCB at 200-300 hPa, while it was at a
604 distance from the WCB at 500-400 hPa. This is consistent with the MOZAIC CO profiles
605 shown in Fig. 5f, suggesting that MOZAIC in fact measured air from the stratosphere at
606 these altitudes. As the wind was stronger in the upper than in the lower troposphere, the
607 WCB-transported CO reached further east in the upper levels (Fig. 15). The simulations
608 suggest that over the boxed area in the MOPITT image in Fig. 4c at 300 hPa, the fire and
609 anthropogenic sources each contributed about ~ 20 % of the observed CO. Comparing the
610 GEOS-Chem simulation (Fig. 14c) with the MOPITT observation (Fig. 4c), we noticed
611 that there were large gaps in MOPITT data north of 35 °N where CO abundances were
612 even higher than the MOPITT measurements south of 35 °N. These gaps were caused by
613 clouds associated with the cyclone system. The complication due to clouds is a problem
614 with an optical instrument like MOPITT, which explains why it is hard to find cases like
615 this in which high CO can be observed by both MOPITT and MOZAIC under a frontal
616 condition.

617 In this case, the strong part of the front (close to the centre of the cyclones) swept
618 southern China, where CO was high (Fig. 13). Along the front (30-40 °N, 100-120 °E),
619 the temperature gradient at 925 hPa was as high as 4.9 C per degree. Strong ascents
620 occurred ahead of the front, with vertical velocity being ~ 0.05 m s⁻¹ at 900 hPa and ~
621 0.20 m s⁻¹ at 750 hPa, and increasing with altitude until 300-250 hPa where the maximum
622 vertical velocity was 0.26 m s⁻¹. Consequently, the high CO can be rapidly lifted to the

623 upper troposphere in this case.

624 FLEXPART was also used to trace down high CO in the MOPITT image by releasing
625 air particles in the boxed area in Fig. 6c (indicated by a bar in Fig. 4c). We found that the
626 most CO came from the southwest part of China (boxed area in Fig. 13) where MOPITT
627 CO composite of 3-10 April 2005 shows high CO of 250-300 ppbv. This CO was lifted
628 along the WCB described above. This agrees with the GEOS-Chem simulation which
629 shows the major contribution of the anthropogenic source to CO in the upper troposphere,
630 likely from the Sichuan Basin (Fig. 15d).

631

632 **5 Discussion**

633 New insights gained from this study and suggestions for future work are discussed as
634 follows.

635 **5.1 Observations of high CO episodes**

636 In the three CO episodes, high CO abundances 300-550 ppbv were observed by
637 MOZAIC in the free troposphere (Fig 5). The elevated CO abundances are among the
638 highest documented at these altitudes in East Asia. Ding et al. (2009) observed high CO
639 episode of ~1185 ppbv at 2.6 km (850-700 hPa) over the North China Plain in summer
640 2007. Nédélec et al. (2005) found CO up to 800 ppbv above 8 km (~400 hPa) near the fire
641 region of Lake Baikal on 3 and 4 June 2003. Highest CO concentrations during
642 TRACE-P were between 250-300 ppbv from 2-12 km (Heald et al., 2003; Liu et al., 2003;
643 Miyazaki et al., 2003). Occurrences of such high CO episodes are not by chance. They
644 reflect the uniqueness and complexity of meteorology, orography, vegetation covers, and
645 CO sources in East Asia. For example, in all the cases, biomass burning occurred from

646 regions with dense vegetation covers and with most active forest fires in East Asia
647 (Schultz, 2002; Duncan et al., 2003). These fires are usually most active in summer in
648 boreal forest in Russia, like in case 2003, and in spring in the southern East Asia, like
649 cases 2004 and 2005, enhancing chances of high CO episodes in these seasons.

650 The frequency of occurrences of such high CO is illustrated in Table 2. As the three
651 cases occurred near Japan, MOZAIC data around the vicinity of Narita from 2001 to
652 2006 are summarized, showing occurrences of various CO abundance ranges in the
653 boundary layer (the surface-850 hPa), the lower (850-600 hPa), middle (600-400 hPa),
654 and upper (400-200 hPa) troposphere. Among all the data in the upper troposphere, CO
655 abundances occurred 93 times (17%) between 200-300 ppbv, 19 times (4%) between
656 300-400 ppbv, and 6 times (1%) over 400 ppbv. In the middle troposphere, the fraction of
657 occurrences of CO within 200-300, 300-400, and over 400 ppbv was 14%, 3%, and 2%,
658 respectively. In the boundary layer, the highest occurrences of CO abundances (38% of
659 all the data in the layer) were within 200-300 ppbv, while the range was within
660 100-200 ppbv in the lower (47%), middle (74%), and upper troposphere (66%).
661 Seasonally, there were more high CO occurrences in the higher altitudes in spring and
662 summer than in fall and winter.

663 The frequency of such high CO episodes is also examined in the GEOS-Chem
664 simulations and MOPITT observations in the vicinity of Narita (126-140 °E 30-40 °N) in
665 2005 (Table 3). For the GEOS-Chem simulations, a count is added to a CO range if the
666 daily maximum CO in the area at a layer falling into that CO range. Thus, the total counts
667 for all the CO ranges at a given layer are 365, while the counts are 281 for MOPITT due
668 to missing data. To minimize noise in daily MOPITT data, only when there were at least

669 10 data with the maximum CO values falling into a given CO range, a count is added.
670 GEOS-Chem can simulate CO up to 400 ppbv in the upper troposphere, while the
671 maximum CO in MOPITT data is lower so that different CO ranges are used in Table 3.
672 Overall, MOZAIC, MOPITT and GEOS-Chem all show a high frequency of high CO
673 (larger than 200 ppbv) at the surface, gradually shifting to a high frequency of low CO
674 (less than 200 ppbv) at the upper troposphere. Between 400-200 hPa, CO episodes with
675 200-300 ppbv occurred 1.2 times every 10 days in GEOS-Chem, slightly lower than in
676 MOPITT (1.8 times) and MOZAIC (1.7 times). Overall, MOZAIC observes 2-5% more
677 transport of high CO to the upper troposphere than GEOS-Chem, while the latter
678 simulates 10-20% more transport of CO (with lower abundances) to the middle and lower
679 troposphere.

680 It is likely that on average, the extremely high CO episodes like the three cases (Fig.
681 5) occurred 2-4 times per 100 days in their respective altitudes over the East China Sea
682 and the Sea of Japan (Tables 2 and 3). As stated, air mass with lower CO abundances of
683 200-300 ppbv can be transported to 400-200 hPa in a frequency of 1-2 times per 10 days
684 (Tables 2 and 3). The frequency can be even higher in spring and summer (Table 2),
685 approximately once a week. Significant impacts of such transport can be expected on the
686 air quality downwind and on the global climate. The transport mechanisms and CO
687 source contributions revealed in this study can also be applicable for these CO episodes,
688 even with lower CO abundances or at lower altitudes.

689

690 **5.2 The role of topography**

691 East Asia's topography varies significantly across its vast width, increasing from east

692 to west, with a variety of terrains. This study found that topography there affected the
693 three cases in different ways. In addition to its general function in orographic lifting (in
694 case 2004), topography also interplay with frontal systems and enhance the uplifting
695 substantially in the North China Plain (in cases 2004 and 2005). Under the influence of
696 the Tibetan Plateau, the southwest vortex (or the Sichuan low) is formed (Tao and Ding,
697 1981) and can facilitate strong convection in the Sichuan basin (in case 2005).

698 In particular, topography-induced convection due to the leeside troughs east of the
699 Hengduan Mountains, proposed by Lin et al. (2009), offers a new mechanism for vertical
700 transport of pollutions from the region (in case 2004). Lin et al. (2009) mainly aimed at
701 vertical transport of pollutions to the lower and middle troposphere. Extending from Lin
702 et al. (2009), this study found it possible to explain pollution transport to the upper
703 troposphere using such a mechanism.

704

705 **5.3 The implications of WCB trends on uplifting of CO**

706 Extratropical cyclones and associated frontal activities are important in lifting CO
707 from the boundary layer to the free troposphere. This also applies to other air pollution.
708 Zhao et al. (2008) found that the influence of Asian dust storms on North American
709 ambient particulate matter levels is highly related to the height to which the frontal
710 cyclones in East Asia can lift dust. Although the functions and characteristics of WCBs
711 have been recognized by earlier studies, this study provides some details unique for the
712 three cases. In case 2004, we found that it is the interplay of the leeside troughs and the
713 cyclone in the northeast of China which formed a front system that transported CO from
714 the Indochina peninsula upward. This case also appeared the most southerly among the

715 three, leading to a most southerly outflow. In case 2005, we found downwelling of
716 stratospheric clean air on the back side of cyclones. We also found that anthropogenic CO
717 from two regions and CO from biomass burning dominated different parts of a WCB. The
718 source allocation was sensitive to the location of the front. Comparing cases 2004 and
719 2005, we found that when large CO source coincided with the strongest part of a WCB,
720 uplifting of CO to the upper troposphere became more possible.

721 In East Asia, cyclones occur most frequently in two regions in spring and summer:
722 one over the lee sides of the Altai-Sayan and the other in the East China Sea and the Sea
723 of Japan (Chen et al., 1991; Yue and Wang, 2008). These are the locations and seasons
724 where and when we can expect similar events to happen in the future. Chen et al. (1991)
725 suggested a decline in cyclonic events in East Asia from 1957 to 1977 and no such
726 decline from 1977 to 1987. Recently, an analysis for a longer term from 1951 to 2010
727 based on ensembles of Twentieth Century Reanalysis (20CR) showed a decreasing trend
728 in the northern part of the Sea of Japan and an increasing trend over the southern part of
729 the Sea of Japan and the leeside of the Altai-Sayan in summer (Wang et al., 2013). The
730 implications of these trends on uplifting of CO deserve further investigation. It would be
731 helpful to conduct statistical analysis of the CO source distribution along WCBs in East
732 Asia in the future.

733

734 **5.4 Comparison between observations from aircraft and satellite and** 735 **model simulations**

736 Pollution transport can be tracked computationally with Euler and Lagrangian
737 approaches, as represented by GEOS-Chem and FLEXPART models, respectively.

738 GEOS-Chem can not only track transport of CO (a physical process) but also consider
739 chemical reactions during the transport while FLEXPART can visualize transport
740 pathways and pin down source regions effectively, without considering chemical
741 functions in the meantime. GEOS-Chem can also fill the gaps in MOPITT satellite data
742 (Figs. 10, 11, and 14). This study found that GEOS-Chem simulated the observed aircraft
743 and satellite CO well in cases 2004 and 2005 but cannot fully reproduce the elevated CO
744 in MOZAIC data in case 2003. The CO plume is simulated in lower mixing ratios at
745 lower altitudes than in the MOZAIC data. The plume also appeared further north. This is
746 possibly due to an underestimated fire inventory or conservative parameterizations in
747 simulating large forest fires or both in GEOS-Chem. Nassar et al. (2009) reported
748 underestimates of CO by GEOS-Chem over the 2006 Indonesia fire region, in
749 comparison with the Tropospheric Emission Spectrometer (TES) observations.
750 FLEXPART can generally simulate the three cases, strikingly well sometimes in
751 agreement with observed details in space and time, although discrepancies between
752 FLEXPART and satellite and aircraft observations can be found in various places on
753 small scales. FLEXPART is good at simulating strong sources, while weak sources
754 sometimes are ignored.

755

756 **5.5 Applications of MOPITT data**

757 We analyzed MOPITT data from two aspects: vertical sensitivity on the synoptic
758 scale. Both are challenging and have not been studied adequately.

759 Large gaps due to clouds and the limited MOPITT swath make application of
760 MOPITT on the synoptic scale difficult. Thus application of MOPITT data over East

761 Asia were mostly focused on monthly or seasonal scales (Tanimoto et al., 2008; Zhao et
762 al., 2010; Hao et al., 2011; Liu et al., 2011; Zhou et al., 2013; Su et al., 2014). This study
763 shows that even with large gaps, daily MOPITT data can capture vertical disturbances of
764 CO on the synoptic scale, which are usually diluted on longer time scales. This study also
765 suggests the importance of filling the gaps with other satellite data or in designing new
766 satellite instruments, for the purpose of detecting such variation over large area on the
767 regional and global scales.

768 Typically for satellite remote sensing products, the MOPITT retrieval at a specific
769 pressure level is influenced by CO from other levels and thus its retrieval at that pressure
770 level can be bias. However, MOPITT can more accurately measure average CO mixing
771 ratio over a thick layer. This results in a coarse vertical resolution and the vertical
772 variation in CO seemed not to be fully resolved in earlier applications of MOPITT data
773 (Jacob et al., 2003). This study addressed the MOPITT vertical sensitivity with newly
774 MOPITT V5 data and found enhanced vertical sensitivity in V5 data in the free
775 troposphere, even the upper troposphere, in addition to in the boundary layer emphasized
776 by Worden et al. (2010) and Deeter et al. (2012). The enhanced DFSs and the averaging
777 kernels in V5 illustrated by Worden et al., (2010) and Deeter et al. (2012) are supported
778 (Fig. 3 and Sect.3).

779 In Fig. 5, the smoothed MOZAIC profiles were calculated using the averaging
780 kernels and the a priori in an area upwind of the MOZAIC measurement within 0-5 °
781 distance for each case as there were no MOPITT data available at the locations of the
782 MOZAIC measurements. Although this may introduce some bias, the averaging kernel
783 smoothed MOZAIC profiles in V5 show more vertical structure in CO than an earlier

784 version of MOPITT data in Jacob et al. (2003). The detection of high CO in the upper
785 troposphere in case 2005 makes MOPITT data promising in studying vertical transport of
786 CO or the vertical distribution of CO qualitatively up to that level. Overall, this study
787 found: (1) MOPITT can differentiate the magnitude of different CO plumes (Figs. 5 and
788 6), (2) MOPITT can distinguish elevated CO in the lower, middle, and upper troposphere
789 (Figs. 5 and 6), (3) the shape of CO plumes in vertical direction matches with simulations
790 of GEOS-Chem and FLEXPART, sometimes remarkably well (Fig.6), and (4) there is
791 more vertical structure in CO in new V5 than in earlier versions of MOPITT data (Fig. 5).

792 It is the relative variations in MOPITT CO data that help diagnose of CO transport
793 vertically or horizontally. This study suggests using MOPITT data quantitatively with
794 caution, especially at altitudes with high CO plumes, as illustrated that the magnitude of
795 elevated CO in MOPITT retrievals can be lower than in the MOZAIC data at altitudes
796 where CO peaked (Fig. 5). Therefore, the vertical variation of CO, even enhanced in V5,
797 is still much smoothed in MOPITT data. MOPITT can distinguish elevated CO in
798 different layers of the free troposphere, yet sometimes cannot specify the exact altitude of
799 elevated CO shown in the MOZAIC measurements (Fig. 5). One limitation for MOPITT's
800 application of vertical transport is the complication of clouds, which often accompany
801 frontal systems. As shown in cases 2004 and 2005, CO is usually high in cloudy areas.
802 Therefore, the magnitude of CO abundances can be underestimated by MOPITT in these
803 areas.

804

805 **6 Conclusions**

806 East Asia is characterized by its unique and complex meteorology, topography,

807 vegetation covers, and CO sources. The characteristics are reflected in uplifting of CO
808 illustrated in three high CO episodes during 2003-2005 in this study. Through integrated
809 analyses of observations from the airborne MOZAIC and spaceborne MOPITT
810 instruments and simulations from a trajectory dispersion model FLEXPART (Stohl et al.,
811 2005) and a chemical transport model GEOS-Chem (Bey et al., 2001), this study draws
812 the following conclusions.

- 813 1. In the three CO episodes, high CO abundances of 300-550 ppbv are observed in
814 aircraft MOZAIC data in the free troposphere over the East China Sea and the Sea
815 of Japan. These are among the highest CO abundances ever documented at these
816 altitudes. The three cases occurred in the seasons and at locations where
817 meteorological and CO source conditions are favorable for such episodes. It is
818 likely that on average, such high episodes occur 2-4 times per 100 days at the
819 respective altitudes in the region. CO episodes in lower altitudes and with lower
820 abundance occur more frequently in the region, about 1-4 times every 10 days with
821 200-300 ppbv in 600-400 hPa.
- 822 2. GEOS-Chem and FLEXPART simulations reveal different CO signatures from
823 biomass burning and anthropogenic sources in the CO enhancement in the three
824 cases, reflecting different transport pathways and mechanisms and locations of both
825 sources. In case 2003, CO from large forest fires near Lake Baikal dominated the
826 elevated CO. In case 2004, anthropogenic CO came from the North China Plain
827 and mostly reached ~ 700 hPa near the East China Sea, while CO from biomass
828 burning in Indochina was transported through two separate pathways, leading to
829 two distinct CO enhancements around 700 hPa and 300 hPa. In case 2005, along a

830 WCB over the East China Sea and the Sea of Japan, anthropogenic CO from the
831 North China Plain and from the Sichuan basin prevailed in the northern and
832 southern part of the WCB, while CO from biomass burning in Indochina was
833 mostly distributed in the middle part of the WCB.

834 3. Topography in East Asia influences vertical transport of CO in different ways. In
835 particular, topography-induced leeside troughs east of the Hengduan Mountains
836 over Indochina lead to strong convection. This new mechanism proposed by Lin et
837 al. (2009) is supported by this study in explaining CO transport to the middle
838 troposphere and further extended for CO transport to the upper troposphere. Strong
839 convection from the Sichuan basin also plays an important role in vertically
840 transporting anthropogenic CO. The topography interacting with frontal activities
841 can enhance the vertical transport of CO substantially in North China Plain.

842 4. Extratropical cyclones and associated frontal activities are important mechanism in
843 lifting CO from the boundary layer to the free troposphere, as illustrated by the
844 three cases and earlier studies. East Asia is one of two regions between 25-45 °N
845 with most frequent WCB events (Eckhardt et al., 2004). Inside East Asia, there are
846 two regions where cyclones occur most frequently: one over the lee sides of the
847 Altai-Sayan and the other in the East China Sea and the Sea of Japan, occurring
848 mostly in spring and summer over both regions (Chen et al., 1991). The seasons
849 and locations of the three high CO episodes just match well with these two areas
850 and active cyclone seasons, which may not happen by chance.

851 5. Biomass burning is identified as an important source for all three episodes,
852 suggesting that CO from sporadic fire activities can provide additional CO to less

853 varying anthropogenic emission and enhance chances of high CO episodes. The
854 fire regions shown in this study are the places with dense vegetation covers and
855 with most active forest fires in East Asia.

856 6. The MOPITT's vertical sensitivity is found to be enhanced in its new V5 NIR/TIR
857 data in the free troposphere, even in the upper troposphere. The daytime V5 data
858 can detect synoptic disturbances of weather systems on horizontal variation of CO.
859 The data also show more vertical structure than earlier versions and can distinguish
860 CO enhancements at different layers of the troposphere, although the detected high
861 CO is over a broad range in altitudes and lacks detailed vertical structure in
862 comparison with the aircraft observations. Because the CO retrieval at a certain
863 pressure level is often smoothed by CO from other levels, the MOPITT retrievals
864 usually underestimate elevated CO peaks at altitudes with high CO plumes. The
865 complication of clouds within frontal systems can generate large gaps in MOPITT
866 data and cause underestimation of CO statistically in these regions. Nevertheless,
867 MOPITT data may be used to qualitatively help diagnose vertical transport
868 processes, with caution on their absolute CO values. On average, MOPITT slightly
869 overestimates the background CO in the upper troposphere.

870

871 **Acknowledgements.**

872 The authors gratefully acknowledge the following data and modeling tools. The
873 satellite CO data are provided by the MOPITT team and acquired from the NASA
874 Langley Research Center Atmospheric Science Data Center. The MOZAIC CO data are
875 from the European Commission, Airbus, and the Airlines (Lufthansa, Austrian, Air

876 France) who carry free of charge the MOZAIC equipment and perform the maintenance
877 since 1994. The Final Analysis Data (FNL) were obtained from NOAA CDC. The
878 GEOE-Chem model is developed and managed by the Atmospheric Chemistry Modeling
879 Group at Harvard University with support from the NASA Atmospheric Chemistry
880 Modeling and Analysis Program (ACMAP). The FLEXPART model development team
881 consists of Andreas Stohl, Sabine Eckhardt, Harald Sodemann, and John Burkhart at the
882 Norwegian Institute for Air Research (NILU). Insights and critiques from two
883 anonymous reviewers are highly appreciated. Financial support is provided by an open
884 fund from the Institute of Remote Sensing and Digital Earth, Chinese Academy of
885 Sciences (OFSLRSS201107), the Key Basic Research Program (2010CB950704,
886 2014CB441203), and the Natural Science Foundation of China (41375140).

887

888 **References**

889

890 Banic, C. M., Isaac, G. A., Cho, H. R., and Iribane, J. V.: The distribution of pollutants
891 near a frontal surface: a comparison between field experiment and modeling, *Water Air
892 Soil Poll.*, 30, 171-177, 1986.

893

894 Barret, B., Le Flochmoen, E., Sauvage, B., Pavelin, E., Matricardi, M., and Cammas, J. P.:
895 The detection of post-monsoon tropospheric ozone variability over south Asia using IASI
896 data, *Atmos. Chem. Phys.*, 11, 9533-9548, doi:10.5194/acp-11-9533-2011, 2011.

897

898 Berntsen, T. K., Karlsdóttir, S., and Jaffe, D. A.: Influence of Asian emissions on the
899 composition of air reaching the north western United States, *Geophys. Res. Lett.*, 26,
900 2171-2174, doi:10.1029/1999GL900477, 1999.

901

902 Bertschi, I. B., Jaffe, D. A., Jaeglé L., Price, H. U., and Dennison, J. B.: PHOBEA/ITCT
903 2002 airborne observations of trans-Pacific transport of ozone, CO, VOCs and aerosols to
904 the northeast Pacific: impacts of Asian anthropogenic and Siberian Boreal fire emissions,
905 *J. Geophys. Res.*, 109, D23S12, doi:10.1029/2003JD004328, 2004.

906

907 Bethan, S., Vaughan, G., Gerbig, C., Volz-Thoms, A., Richer, H., and Tiddeman, D. A.:
908 Chemical air mass differences near fronts, *J. Geophys. Res.*, 103, 13413-13434, 1998.

909

910 Bey, I., Jacob, D. J., Yantosca, R. M., Logan, J. A., Field, B. D., Fiore, A. M., Li, Q., Liu,
911 H. Y., Mickley, L. J., and Schultz, M. G.: Global modeling of tropospheric chemistry with
912 assimilated meteorology: model description and evaluation, *J. Geophys. Res.*, 106,
913 23073-23095, 2001.

914

915 Brown, R. M., Daum, P. H., Schwartz, S. E., and Hjelmfelt, M. R.: Variations in the
916 chemical composition of clouds during frontal passage, in: *The Meteorology of Acid
917 Deposition*, edited by: Samson, P. J., Air Pollut. Control Assoc., Pittsburgh, Pa., 202-212,
918 1984.

919

920 Chan, D., Yuen, C. W., Higuchi, K., Shashkov, A., Liu, J., Chen, J., and Worthy, D.: On
921 the CO₂ exchange between the atmosphere and the biosphere: the role of synoptic and
922 mesoscale processes, *Tellus B*, 56, 194-212, 2004.

923

924 Chen, B., Xu, X. D., Yang, S., and Zhao, T. L.: Climatological perspectives of air
925 transport from atmospheric boundary layer to tropopause layer over Asian monsoon
926 regions during boreal summer inferred from Lagrangian approach, *Atmos. Chem. Phys.*,
927 12, 5827-5839, doi:10.5194/acp-12-5827-2012, 2012.

928

929 Chen, S., Kuo, Y., Zhong, P., and Bai, Q.: Synoptic climatology of cyclogenesis over East
930 Asia, 1958-1987, *Mon. Weather Rev.*, 119, 1407-1418, 1991.

931

932 Chung, K. K., Chan, J. C. L., Ng, C. N., Lam, K. S., and Wang, T.: Synoptic conditions
933 associated with high carbon monoxide episodes at coastal station in Hong Kong, *Atmos.
934 Environ.*, 33, 3099-3095, 1999.

935

936 Cooper, O. R., Moody, J. L., Parrish, D. D., Trainer, M., Ryerson, T. B., Holloway, J. S.,
937 Hübler, G., Fehsenfeld, F. C., and Evans, M. J.: Trace gas composition of midlatitude
938 cyclones over the western North Atlantic Ocean: a conceptual model, *J. Geophys. Res.*,
939 107, D7, doi:10.1029/2001JD000901, 2002.

940

941 Cooper, O. R., Forster, C., Parrish, D., Dunlea, E., Habler, G., Fehsenfeld, F., Holloway,
942 J., Oltmans, S., Johnson, B., Wimmers, A., and Horowitz, L.: On the life-cycle of a
943 stratospheric intrusion and its dispersion into polluted warm conveyor belts, *J. Geophys.
944 Res.*, 109, D23S09, doi:10.1029/2003JD004006, 2004.

945

946 Cooper, O. R., Stohl, A., Hubler, G., Hsie, E. Y., Parrish, D. D., Tuck, A. F., Kiladis, G.
947 N., Oltmans, S. J., Johnson, B. J., Shapiro, M., Moody, J. L., and Lefohn, A. S.: Direct
948 transport of midlatitude stratospheric ozone into the lower troposphere and marine
949 boundary layer of the tropical Pacific Ocean, *J. Geophys. Res.*, 110, D23310, doi:
950 10.1029/2005JD005783, 2005.

951

952 Cooper, O. R., Stohl, A., Trainer, M., Thompson, A., Witte, J. C., Oltmans, S. J., Johnson,
953 B. J., Merrill, J., Moody, J. L., Tarasick, D., Nédélec, P., Forbes, G., Newchurch, M. J.,
954 Schmidlin, F. J., Johnson, B. J., Turquety, S., Baughcum, S. L., Ren, X., Fehsenfeld, F. C.,
955 Meagher, J. F., Spichtinger, N., Brown, C. C., McKeen, S. A., McDermid, I. S., and

956 Leblanc, T.: Large upper tropospheric ozone enhancements above mid-latitude North
957 America during summer: in situ evidence from the IONS and MOZAIC ozone
958 monitoring network, *J. Geophys. Res.*, 111, D24S05, doi:10.1029/2006JD007306, 2006.
959

960 Cristofanelli, P., Bonasoni, P., Collins, W., Feichter, J., Forster, C., James, P., Kentarchos,
961 A., Kubik, P. W., Land, C., Meloen, J., Roelofs, G. J., Siegmund, P., Sprenger, M.,
962 Schnabel, C., Stohl, A., Tobler, L., Tositti, L., Trickl, T., and Zanis, P.:
963 Stratosphere-to-troposphere transport: a model and method evaluation, STACCATO
964 special section of *J. Geophys. Res.*, 108, 8525, doi:10.1029/2002JD002600, 2003.
965

966 Daley, R.: *Atmospheric Data Analysis*, Cambridge University Press, Cambridge, 1991.
967

968 Damoah, R., Spichtinger, N., Forster, C., James, P., Mattis, I., Wandinger, U., Beirle, S.,
969 Wagner, T., and Stohl, A.: Around the world in 17 days - hemispheric-scale transport of
970 forest fire smoke from Russia in May 2003, *Atmos. Chem. Phys.*, 4, 1311-1321,
971 doi:10.5194/acp-4-1311-2004, 2004.
972

973 Davies, D. K., Ilavajhala, S., Wong, M. M., and Justice, C. O.: Fire information for
974 resource management system: archiving and distributing MODIS active fire data, *IEEE T.*
975 *Geosci. Remote*, 47,72-79, 2009.
976

977 Deeter, M. N., Emmons, L. K., Francis, G. L., Edwards, D. P., Gille, J. C., Warner, J. X.,
978 Khattatov, B., Ziskin, D., Lamarque, J.-F., Ho, S.-P., Yudin, V., Attié J.-L., Packman, D.,
979 Chen, J., Mao, D., and Drummond, J. R.: Operational carbon monoxide retrieval
980 algorithm and selected results for the MOPITT instrument, *J. Geophys. Res.*, 108, 4399,
981 doi:10.1029/2002JD003186, 2003.
982

983 Deeter, M. N., Emmons, L. K., Edwards, D. P., Gille, J. C., and Drummond, J. R.:
984 Vertical resolution and information content of CO profiles retrieved by MOPITT,
985 *Geophys. Res. Lett.*, 31, L15112, doi:10.1029/2004GL020235, 2004.
986

987 Deeter, M. N., Worden, H. M., Edwards, D. P., Gille, J. C., and Andrews, A. E.:
988 Evaluation of MOPITT retrievals of lower-tropospheric carbon monoxide over the United
989 States, *J. Geophys. Res.*, 117, D13306, doi:10.1029/2012JD017553, 2012.
990

991 Deeter, M. N., Martínez-Alonso, S., Edwards, D. P., Emmons, L. K., Gille, J. C., Worden,
992 H. M., Pittman, J. V., Daube, B. C., and Wofsy, S. C.: Validation of MOPITT Version 5
993 thermal-infrared, near-infrared, and multispectral carbon monoxide profile retrievals for
994 2000–2011, *J. Geophys. Res.*, doi:10.1002/jgrd.50272, 2013.
995

996 Dickerson, R. R., Huffman, G. J., Luke, W. T., Nunnermacker, L. J., Pickering, K. E.,
997 Leslie, A. C. D., Lindsey, C. G., Slinn, W. G. N., Kelly, T. J., Daum, P. H., Delany, A. C.,
998 Greenberg, J. P., Zimmerman, P. R., Boatman, J. F., Ray, J. D., and Stedman, D. H.:
999 Thunderstorms – an important mechanism in the transport of air pollutants, *Science*, 235,
1000 4787, 460-464, 1987.
1001

1002 Dickerson, R. R., Li, C., Li, Z., Marufu, L., T., Stehr, J. W., McClure, B., Krotkov, N.,
1003 Chen, H., Wang, P., Xia, X., Ban, X., Gong, F., Yuan, J., and Yang, J.: Aircraft
1004 observations of dust and pollutants over northeast China: insight into the meteorological
1005 mechanisms of transport, *J. Geophys. Res.*, 112, D24S90, doi:10.1029/2007JD008999,
1006 2007.
1007
1008 Ding, A., Wang, T., Xue, L., Gao, J., Stohl, A., Lei, H., Jin, D., Ren, Y., Wang, X., Wei, X.,
1009 Qi, Y., Liu, J., and Zhang, X.: Transport of north China air pollution by midlatitude
1010 cyclones: case study of aircraft measurements in summer 2007, *J. Geophys. Res.*, 114,
1011 D08304, doi:10.1029/2008JD011023, 2009.
1012
1013 Donnell, E. A., Fish, D. J., Dicks, E. M., and Thorpe, A. J.: Mechanisms for pollutant
1014 transport between the boundary layer and the free troposphere, *J. Geophys. Res.*, 106,
1015 7847-7856, 2001.
1016
1017 Drummond, J. R.: Measurements of pollution in the troposphere (MOPITT), in: *The Use*
1018 *of EOS for Studies of Atmospheric Physics*, edited by: Gille, J. C. and Visconti, G., North
1019 Holland, New York, 77-101, 1992.
1020
1021 Drummond, J. R. and Mand, G. S.: The measurements of pollution in the troposphere
1022 (MOPITT) instrument: overall performance and calibration requirements, *J. Atmos.*
1023 *Ocean. Tech.*, 13, 314-320,
1024 1996.
1025
1026 Duncan, B. N., Martin, R. V., Staudt, A. C., Yevich, R., and Logan, J. A.: Interannual and
1027 seasonal variability of biomass burning emissions constrained by satellite observations, *J.*
1028 *Geophys. Res.*, 108, 4040, doi:10.1029/2002JD002378, 2003.
1029
1030 Duncan, B. N., Logan, J. A., Bey, I., Megretskaia, I. A., Yantosca, R. M., Novelli, P. C.,
1031 Jones, N. B., and Rinsland, C. P.: Global budget of CO, 1988-1997: source estimates and
1032 validation with a global model, *J. Geophys. Res.*, 112, D22301,
1033 doi:10.1029/2007JD008459, 2007.
1034
1035 Eckhardt, S., Stohl, A., Wernli, H., James, P., Forster, C., and Spichtinger, N.: A 15-Year
1036 climatology of warm conveyor belts, *J. Climate*, 17, 218-237, 2004.
1037
1038 Edwards, D. P., Halvorson, C. M., and Gille, J. C.: Radiative transfer modeling for the
1039 EOS Terra satellite measurements of pollution in the troposphere (MOPITT instrument), *J.*
1040 *Geophys. Res.*, 104, 16755-16775, 1999.
1041
1042 Emmons, L. K., Deeter, M. N., Gille, J. C., Edwards, D. P., Attie, J.-L., Warner, J., Ziskin,
1043 D., Khattatov, B., Yudin, V., Lamarque, J.-F., Ho, S.-P., Mao, D., Chen, J. S., Drummond,
1044 J., Novelli, P., Sachse, G., Coffey, M. T., Hannigan, J. W., Gerbig, C., Kawakami, S.,
1045 Kondo, Y., Takegawa, N., Baehr, J., and Ziereis, H.: Validation of MOPITT CO retrievals
1046 with aircraft in situ profiles, *J. Geophys. Res.*, 109, D03309, doi:10.1029/2003JD004101,
1047 2004.

1048
1049 Giglio, L., Descloitres, J., Justice, C. O., and Kaufman, Y. J.: An enhanced contextual fire
1050 detection algorithm for MODIS, *Remote Sens. Environ.*, **87**, 273-282, 2003.
1051
1052 Hao, H., Valks, P., Loyola, D., Chen, Y. F., and Zimmer, W.: Space-based measurements
1053 of air quality during the World Expo 2010 in Shanghai, *Environ. Res. Lett.*, **6**, 044004,
1054 doi:10.1088/1748-9326/6/4/044004, 2011.
1055
1056 He, H., Tarasick, D. W., Hocking, W. K., Carey-Smith, T. K., Rochon, Y., Zhang, J.,
1057 Makar, P. A., Osman, M., Brook, J., Moran, M. D., Jones, D. B. A., Mihele, C., Wei, J. C.,
1058 Osterman, G., Argall, P. S., McConnell, J., and Bourqui, M. S.: Transport analysis of
1059 ozone enhancement in Southern Ontario during BAQS-Met, *Atmos. Chem. Phys.*, **11**,
1060 2569-2583, doi:10.5194/acp-11-2569-2011, 2011.
1061
1062 Heald, C. L., Jacob, D. J., Fiore, A. M., Emmons, L. K., Gille, J. C., Deeter, M. N.,
1063 Warner, J., Edwards, D. P., Crawford, J. H., Hamlin, A. J., Sachse, G. W., Browell, E. V.,
1064 Avery, M. A., Vay, S. A., Westberg, D. J., Blake, D. R., Singh, H. B., Sandholm, S. T.,
1065 Talbot, R. W., and Fuelberg, H. E.: Asian outflow and transpacific transport of carbon
1066 monoxide and ozone pollution: an integrated satellite, aircraft and model perspective, *J.*
1067 *Geophys. Res.*, **108**, 4804, doi:10.1029/2003JD003507, 2003.
1068
1069 Hocking, W. K., Carey-Smith, T. K., Tarasick, D. W., Argall, P. S., Strong, K., Rochon, Y.,
1070 Zawadzki, I., and Taylor, P. A.: Detection of stratospheric ozone intrusion by wind
1071 profiler radars, *Nature*, **450**, 281-284, doi:10.1038/nature06312, 2007.
1072
1073 Holloway, T., Levy II, H., and Kasibhatla, P.: Global distribution of carbon monoxide, *J.*
1074 *Geophys. Res.*, **105**, 12123-12147, doi:10.1029/1999JD901173, 2000.
1075
1076 Jacob, D. J.: *Introduction to Atmospheric Chemistry*, Princeton University Press,
1077 Princeton, New Jersey, 1999.
1078
1079 Jacob, D. J., Crawford, J. H., Kleb, M. M., Connors, V. S., Bendura, R. J., Raper, J. L.,
1080 Sachse, G. W., Gille, J. C., Emmons L., and Heald, C. L.: Transport and Chemical
1081 Evolution over the Pacific (TRACE-P) aircraft mission: design, execution, and first
1082 results, *J. Geophys. Res.*, **108**, 9000, doi:10.1029/2002JD003276, 2003.
1083
1084 Jaffe, D., Anderson, T., Covert, D., Kotchenruther, R., Trost, B., Danielson, J., Simpson,
1085 W., Berntsen, T., Karlsdottir, S., Blake, D., Harris, J., Carmichael, G., and Uno, I.:
1086 Transport of Asian air pollution to North America, *Geophys. Res. Lett.*, **26**, 711-714,
1087 1999.
1088
1089 Jaffe, D., Bertschi, I., Jaegle, L., Novelli, P., Reid, J. S., Tanimoto, H., Vingarzan, R., and
1090 Westphal, D. L.: Long-range transport of Siberian biomass burning emissions and impact
1091 on surface ozone in western North America, *Geophys. Res. Lett.*, **31**, L16106,
1092 doi:10.1029/2004GL020093, 2004.
1093

1094 Jiang, Z., Jones, D. B. A., Kopacz, M., Liu, J., Henze, D. K., and Heald, C.: Quantifying
1095 the impact of model errors on top-down estimates of carbon monoxide emissions using
1096 satellite observations, *J. Geophys. Res.* 116, D15306, doi:10.1029/2010JD015282, 2011.
1097

1098 Jones, D. B. A., Bowman, K. W., Logan, J. A., Heald, C. L., Liu, J., Luo, M., Worden, J.,
1099 and Drummond, J.: The zonal structure of tropical O₃ and CO as observed by the
1100 Tropospheric Emission Spectrometer in November 2004 - Part 1: Inverse modeling of CO
1101 emissions, *Atmos. Chem. Phys.*, 9, 3547-3562, doi:10.5194/acp-9-3547-2009, 2009.
1102

1103 Justice, C. O., Giglio, L., Korontzi, S., Owens, J., Morisette, J. T., Roy, D., Descloitres, J.,
1104 Alleaume, S., Petitcolin, F., and Kaufman, Y.: The MODIS fire products, *Remote Sens.*
1105 *Environ.*, 83, 244-262, 2002.
1106

1107 Kar, J., Bremer, H., Drummond, J. R., Rochon, Y. J., Jones, D. B. A., Nichitiu, F., Zou, J.,
1108 Liu, J., Gille, J. C., Edwards, D. P., Deeter, M. N., Francis, G., Ziskin, D., and Warner, J.:
1109 Evidence of vertical transport of carbon monoxide from measurements of pollution in the
1110 troposphere (MOPITT). *Geophys. Res. Lett.*, 31, L23105, doi:10.1029/2004GL021128,
1111 2004.
1112

1113 Kar, J., Drummond, J. R., Jones, D. B. A., Liu, J., Nichitiu, F., Zou, J., Gille, J. C.
1114 Edwards, D. P., Deeter, M. N.: Carbon monoxide (CO) maximum over the Zagros
1115 mountains in the Middle East: signature of mountain venting?, *Geophys. Res. Lett.*, 33,
1116 L15819, doi:10.1029/2006GL026231, 2006.
1117

1118 Kar, J., Jones, D. B. A., Drummond, J. R., Attie, J. L., Liu, J., Zou, J., Nichitiu, F.,
1119 Seymour, M. D., Edwards, D. P., Deeter, M. N., Gille, J. C., and Richter, A.:
1120 Measurement of low-altitude CO over the Indian subcontinent by MOPITT, *J. Geophys.*
1121 *Res.*, 113, D16307, doi:10.1029/2007JD009362, 2008.
1122

1123 Kopacz, M., Jacob, D. J., Fisher, J. A., Logan, J. A., Zhang, L., Megretskaia, I. A.,
1124 Yantosca, R. M., Singh, K., Henze, D. K., Burrows, J. P., Buchwitz, M., Khlystova, I.,
1125 McMillan, W. W., Gille, J. C., Edwards, D. P., Eldering, A., Thouret, V., and Nédélec, P.:
1126 Global estimates of CO sources with high resolution by adjoint inversion of multiple
1127 satellite datasets (MOPITT, AIRS, SCIAMACHY, TES), *Atmos. Chem. Phys.*, 10,
1128 855-876, doi:10.5194/acp-10-855-2010, 2010.
1129

1130 Kowol-Santen, J., Beekmann, M., Schmitgen, S., and Dewey, K.: Tracer analysis of
1131 transport from the boundary layer to the free atmosphere, *Geophys. Res. Lett.*, 28,
1132 2907-2910, 2001.
1133

1134 Lavoué D., Lioussé, C., Cachier, H., Stocks, B. J., and Goldammer, J. G.: Modeling of
1135 carbonaceous particles emitted by boreal and temperate wildfires at northern latitudes, *J.*
1136 *Geophys. Res.*, 105, 26871-26890, doi:10.1029/2000JD900180, 2000.
1137

1138 Lawrence, M. G., Rasch, P. J., von Kuhlmann, R., Williams, J., Fischer, H., de Reus, M.,
1139 Lelieveld, J., Crutzen, P. J., Schultz, M., Stier, P., Huntrieser, H., Heland, J., Stohl, A.,

1140 Forster, C., Elbern, H., Jakobs, H., and Dickerson, R. R.: Global chemical weather
1141 forecasts for field campaign planning: predictions and observations of large-scale features
1142 during MINOS, CONTRACE, and INDOEX, *Atmos. Chem. Phys.*, 3, 267-289,
1143 doi:10.5194/acp-3-267-2003, 2003.
1144

1145 Li, Q. B., Jacob, D. J., Park, R. J., Wang, Y. X., Heald, C. L., Hudman, R., Yantosca, R.
1146 M., Martin, R. V., and Evans, M. J.: North American pollution outflow and the trapping
1147 of convectively lifted pollution by upper-level anticyclone, *J. Geophys. Res.*, 110,
1148 D10301, doi:10.1029/2004JD005039, 2005.
1149

1150 Li, Z., Chen, H., Cribb, M., Dickerson, R., Holben, B., Li, C., Lu, D., Luo, Y., Maring, H.,
1151 Shi, G., Tsay, S.-C., Wang, P., Wang, Y., Xia, X., Zheng, Y., Yuan, T., and Zhao, F.:
1152 Preface to special section on East Asian Studies of Tropospheric Aerosols: an
1153 International Regional Experiment (EAST-AIRE), *J. Geophys. Res.*, 112, D22S00,
1154 doi:10.1029/2007JD008853, 2007.
1155

1156 Liang, Q., Jaegle, L., Jaffe, D. A., Weiss-Penzias, P., Heckman, A., and Snow, J. A.:
1157 Long-range transport of Asian pollution to the northeast Pacific: seasonal variations and
1158 transport pathways of carbon monoxide, *J. Geophys. Res.*, 109, D23S07,
1159 doi:10.1029/2003JD004402, 2004.
1160

1161 Lin, C.-Y., Hsu, H.-m., Lee, Y. H., Kuo, C. H., Sheng, Y.-F., and Chu, D. A.: A new
1162 transport mechanism of biomass burning from Indochina as identified by modeling
1163 studies, *Atmos. Chem. Phys.*, 9, 7901-7911, doi:10.5194/acp-9-7901-2009, 2009.
1164

1165 Liu, C., Beirle, S., Butler, T., Liu, J., Hoor, P., Jöckel, P., Penning de Vries, M., Pozzer, A.,
1166 Frankenberg, C., Lawrence, M. G., Lelieveld, J., Platt, U., and Wagner, T.: Application of
1167 SCIAMACHY and MOPITT CO total column measurements to evaluate model results
1168 over biomass burning regions and Eastern China, *Atmos. Chem. Phys.*, 11, 6083-6114,
1169 doi:10.5194/acp-11-6083-2011, 2011.
1170

1171 Liu, H. Y., Jacob, D. J., Bey, I., Yantosca, R. M., Duncan, B. N., and Sachse, G.W.:
1172 Transport pathways for Asian combustion outflow over the Pacific: interannual and
1173 seasonal variations, *J. Geophys. Res.*, 108, 8786, doi:10.1029/2002JD003102, 2003.
1174

1175 Liu, J., Drummond, J. R., Li, Q., Gille, J. C., and Ziskin, D. C.: Satellite mapping of CO
1176 emission from forest fires in northwest America using MOPITT measurements, *Remote
1177 Sens. Environ.*, 95, 502-516, 2005.
1178

1179 Liu, J., Drummond, J. R., Jones, D. B. A., Cao, Z., Bremer, H., Kar, J., Zou, J., Nichitiu,
1180 F., and Gille, J. C.: Large horizontal gradients in atmospheric CO at the synoptic scale as
1181 seen by spaceborne measurements of pollution in the troposphere, *J. Geophys. Res.*, 111,
1182 D02306, doi:10.1029/2005JD006076, 2006.
1183

1184 Mari, C., Evans, M. J., Palmer, P. I., Jacob, D. J., and Sachse, G. W.: Export of Asian
1185 pollution during two cold front episodes of the TRACE-P experiment, *J. Geophys. Res.*,

1186 109, D15S17, doi:10.1029/2003JD004307, 2004.
1187
1188 Miyazaki, Y., Kondo, Y., Koike, M., Fuelberg, H. E., Kiley, C. M., Kita, K., Takegawa, N.,
1189 Sachse, G. W., Flocke, F., Weinheimer, A. J., Singh, H. B., Eisele, F. L., Zondlo, M.,
1190 Talbot, R. W., Sandholm, S. T., Avery, M. A., and Blake, D. R.: Synoptic-scale transport
1191 of reactive nitrogen over the western Pacific in spring, *J. Geophys. Res.*, 108, 8788,
1192 doi:10.1029/2002JD003248, 2003.
1193
1194 Marenco, A., Thouret, V., Nédélec, P., Smit, H., Helten, M., Kley, D., Karcher, F., Simon,
1195 P., Law, K., Pyle, J., Poschmann, G., Wrede, R. V., Hume, C., and Cook, T: Measurement
1196 of ozone and water vapor by Airbus in-service aircraft: the MOZAIC airborne program,
1197 An overview, *J. Geophys. Res.*, 103, 25631-25642, 1998.
1198
1199 Nassar, R., Logan, J. A., Megretskaia, I. A., Murray, L. T., Zhang, L., and Jones, D. B. A.:
1200 Analysis of tropical tropospheric ozone, carbon monoxide, and water vapor during the
1201 2006 El Niño using TES observations and the GEOS-Chem model, *J. Geophys. Res.*, 114,
1202 D17304, doi:10.1029/2009JD011760, 2009.
1203
1204 Nassar, R., Jones, D. B. A., Suntharalingam, P., Chen, J. M., Andres, R. J., Wecht, K. J.,
1205 Yantosca, R. M., Kulawik, S. S., Bowman, K. W., Worden, J. R., Machida, T., and
1206 Matsueda, H.: Modeling global atmospheric CO₂ with improved emission inventories and
1207 CO₂ production from the oxidation of other carbon species, *Geosci. Model Dev.*, 3,
1208 689-716, doi:10.5194/gmd-3-689-2010, 2010.
1209
1210 Nédélec, P., Thpuret, V., Brioude, J., Sauvage, B., Cammas, J., Stohl, A.: Extreme CO
1211 concentrations in the upper troposphere over northeast Asia in June 2003 from the in situ
1212 MOZAIC aircraft data, *Geophys. Res. Lett.*, 32, L14807, doi:10.1029/2005GL023141,
1213 2005.
1214
1215 Novelli, P., Masarie, K. A., and Lang, P. M.: Distributions and recent changes of carbon
1216 monoxide in the lower troposphere, *J. Geophys. Res.*, 103, 19015 - 19033, 1998.
1217
1218 Olivier, J. G. J. and Berdowski, J. J. M.: Global emission sources and sinks, in: *The*
1219 *Climate System*, edited by: Berdowski, J., Guicherit, R., and Heij, B. J., Swets &
1220 Zeitlinger, Lisse, the Netherlands, 33 -77, 2001.
1221
1222 Oltmans, S. J., Lefohn, A. S., Harris, J. M., Tarasick, D. W., Thompson, A. M.,
1223 Wernli, H., Johnson, B. J., Novelli, P. C., Montzka, S. A., Ray, J. D., Patrick, L. C.,
1224 Sweeney, C., Jefferson, A., Dann, T., Davies, J., Shapiro, M., Holben, B. N.: Enhanced
1225 ozone over western North America from biomass burning in Eurasia during April 2008 as
1226 seen in surface and profile observations, *Atmos. Environ.*, 44, 4497-4509, 2010.
1227
1228 Pan, L., Gille, J. C., Edwards, D. P., Bailey, P. L., and Rodgers, C. D.: Retrieval of
1229 tropospheric carbon monoxide for the MOPITT experiment, *J. Geophys. Res.*, 103,
1230 32277-32290, 1998.
1231

1232 Pickering, K. E., Dickerson, R. R., Huffman, G. J., Boatman, J. F., and Schanot, A.: Trace
1233 gas transport in the vicinity of frontal convective clouds, *J. Geophys. Res.*, 93, 759 -773,
1234 doi:10.1029/JD093iD01p00759, 1998.
1235

1236 Randel, W. J., Park, M., Emmons, L., Kinnison, D., Bernath, P., Walker, K. A., Boone, C.,
1237 and Pumphrey, H.: Asian monsoon transport of pollution to the stratosphere, *Science*, 328,
1238 611-613, doi:10.1126/science.1182274, 2010.
1239

1240 Rogers, C. D.: *Inverse Methods for Atmospheric Sounding, Theory and Practice*, World
1241 Sci., River Edge, N.J., 2000.
1242

1243 Schultz, M. G.: On the use of ATSR fire count data to estimate the seasonal and
1244 interannual variability of vegetation fire emissions, *Atmos. Chem. Phys.*, 2, 387-395,
1245 doi:10.5194/acp-2-387-2002, 2002.
1246

1247 Stohl, A.: A 1-year Lagrangian "climatology" of airstreams in the North Hemisphere
1248 troposphere and lowermost stratosphere, *J. Geophys. Res.*, 106, 7263-7279, 2001.
1249

1250 Stohl, A., Hittenberger, M., and Wotawa, G.: Validation of the Lagrangian particle
1251 dispersion model FLEXPART against large scale tracer experiment data, *Atmos. Environ.*,
1252 24, 4245-4264, 1998.
1253

1254 Stohl, A., Eckhardt, S., Forster, C., James, P., and Spichtinger, N.: On the pathways and
1255 timescales of intercontinental air pollution transport, *J. Geophys. Res.*, 107, 4684,
1256 doi:10.1029/2001JD001396, 2002.
1257

1258 Stohl, A., Forster, C., Frank, A., Seibert, P., and Wotawa, G.: Technical note: The
1259 Lagrangian particle dispersion model FLEXPART version 6.2, *Atmos. Chem. Phys.*, 5,
1260 2461-2474, doi:10.5194/acp-5-2461-2005, 2005.
1261

1262 Streets, D. G., Zhang, Q., Wang, L., He, K., Hao, J., Wu, Y., Tang, Y., and Carmichael, G.
1263 R.: Revisiting China's CO emissions after the Transport and Chemical Evolution over the
1264 Pacific (TRACE-P) mission: synthesis of inventories, atmospheric modeling, and
1265 observations, *J. Geophys. Res.*, 111, D14306, doi:10.1029/2006JD007118, 2006.
1266

1267 Su, M., Lin, Y., Fan, X., Peng, L., Zhao, C.: Impacts of global emissions of CO, NO_x, and
1268 CH₄ on China tropospheric hydroxyl free radicals, *Adv. Atmos. Sci.*, 29, 4, 838-854,
1269 2012.
1270

1271 Suntharalingam, P., Jacob, D. J., Palmer, P. I., Logan, J. A., Yantosca, R. M., Xiao, Y.,
1272 Evans, M. J., Streets, D., Vay, S. A., and Sachse, G.: Improved quantification of Chinese
1273 carbon fluxes using CO₂/CO correlations in Asian outflow, *J. Geophys. Res.*, 109,
1274 D18S18, doi:10.1029/2003JD004362, 2004.
1275

1276 Tao, S. and Ding, Y.: Observational evidence of the influence of the Qinghai-Xizang
1277 (Tibet) Plateau on the occurrence of heavy rain and severe convective storms in China, B.

1278 Am. Meteorol. Soc., 62, 2-30, 1981.
1279
1280 Tanimoto, H., Sawa, Y., Yonemura, S., Yumimoto, K., Matsueda, H., Uno, I., Hayasaka,
1281 T., Mukai, H., Tohjima, Y., Tsuboi, K., and Zhang, L.: Diagnosing recent CO emissions
1282 and ozone evolution in East Asia using coordinated surface observations, adjoint inverse
1283 modeling, and MOPITT satellite data, *Atmos. Chem. Phys.*, 8, 3867-3880,
1284 doi:10.5194/acp-8-3867-2008, 2008.
1285
1286 Tsutsumi, Y., Makino, Y., and Jensen, J. B.: Vertical and latitudinal distributions of
1287 tropospheric ozone over the western Pacific: case studies from the PACE aircraft
1288 missions, *J. Geophys. Res.*, 108, 4251, doi:10.1029/2001JD001374, 2003.
1289
1290 van der Werf, G. R., Randerson, J. T., Giglio, L., Collatz, G. J., Mu, M., Kasibhatla, P. S.,
1291 Morton, D. C., DeFries, R. S., Jin, Y., and van Leeuwen, T. T.: Global fire emissions and
1292 the contribution of deforestation, savanna, forest, agricultural, and peat fires (1997-2009),
1293 *Atmos. Chem. Phys.*, 10, 11707--11735, doi:10.5194/acp-10-11707-2010, 2010.
1294
1295 Wang, T., Nie, W., Gao, J., Xue, L. K., Gao, X. M., Wang, X. F., Qiu, J., Poon, C. N.,
1296 Meinardi, S., Blake, D., Wang, S. L., Ding, A. J., Chai, F. H., Zhang, Q. Z., and Wang, W.
1297 X.: Air quality during the 2008 Beijing Olympics: secondary pollutants and regional
1298 impact, *Atmos. Chem. Phys.*, 10, 7603-7615, doi:10.5194/acp-10-7603-2010, 2010.
1299
1300 Wang, X. L., Feng, Y., Compo, G. P., Swail, V. R., Zwiers, F. W., Allan, R. J., and
1301 Sardeshmukh, P. D.: Trends and low frequency variability of extra-tropical cyclone
1302 activity in the ensemble of twentieth century reanalysis, *Clim. Dynam.*, 40, 2775-2800,
1303 doi:10.1007/s00382-012-1450-9, 2013.
1304
1305 Wofsy, S. C., and the HIPPO Science Team and Cooperating Modellers and Satellite
1306 Teams: HIAPER pole-to-pole observations (HIPPO): Fine-grained, global-scale
1307 measurements of climatically important atmospheric gases and aerosols, *Phil. Trans. R.*
1308 *Soc. A*, 369, 2073–2086, doi:10.1098/rsta.2010.0313, 2011.
1309
1310 Worden, H. M., Deeter, M. N., Edwards, D. P., Gille, J. C., Drummond, J. R., and
1311 Nédélec, P.: Observations of near-surface carbon monoxide from space using MOPITT
1312 multispectral retrievals, *J. Geophys. Res.*, 115, D18314, doi:10.1029/2010JD014242,
1313 2010.
1314
1315 Wotawa, G., Novelli, P. C., Trainer, M., and Granier, C.: Interannual variability of
1316 summertime CO concentrations in the Northern Hemisphere explained by boreal forest
1317 fires in North America and Russia, *Geophys. Res. Lett.*, 28, 4575-4578, 2001.
1318
1319 Yienger, J. J., Galanter, M., Holloway, T. A., Phadnis, M. J., Guttikunda, S. K.,
1320 Carmichael, G. R., Moxim, W. J., and Levy II, H.: The episodic nature of air pollution
1321 transport from Asia to North America, *J. Geophys. Res.*, 105, 26931-26945,
1322 doi:10.1029/2000JD900309, 2000.
1323

1324 Yu, R., Xu, Y., Zhou, T., and Li, J.: Relation between rainfall duration and diurnal
1325 variation in the warm season precipitation over central eastern China, *Geophys. Res. Lett.*,
1326 34, L13703, doi:10.1029/2007GL030315, 2007.

1327

1328 Yue, X. and Wang, H.: The springtime North Asia cyclone activity index and the
1329 Southern Annular Mode, *Adv. Atmos. Sci.*, 25, 673-679, 2008.

1330

1331 Yurganov, L. N., McMillan, W. W., Dzhola, A. V., Grechko, E. I., Jones, N. B., and van
1332 der Werf, G.: Global AIRS and MOPITT CO measurements: validation, comparison, and
1333 links to biomass burning variations and carbon cycle, *J. Geophys. Res.*, 113, D09301,
1334 doi:10.1029/2007JD009229, 2008.

1335

1336 Zhang, L., Jacob, D. J., Bowman, K. W., Logan, J. A., Turquety, S., Hudman, R. C., Li, Q.
1337 B., Beer, R., Worden, H. M., Worden, J. R., Rinsland, C. P., Kulawik, S. S., Lampel, M.
1338 C., Shephard, M. W., Fisher, B. M., Eldering, A., and Avery, M. A.: Ozone-CO
1339 correlations determined by the TES satellite instrument in continental outflow regions,
1340 *Geophys. Res. Lett.*, 33, L18804, doi:10.1029/2006GL026399, 2006.

1341

1342 Zhang, Q., Streets, D. G., Carmichael, G. R., He, K. B., Huo, H., Kannari, A., Klimont, Z.,
1343 Park, I. S., Reddy, S., Fu, J. S., Chen, D., Duan, L., Lei, Y., Wang, L. T., and Yao, Z. L.:
1344 Asian emissions in 2006 for the NASA INTEX-B mission, *Atmos. Chem. Phys.*, 9,
1345 5131-5153, doi:10.5194/acp-9-5131-2009, 2009.

1346

1347 Zhao, C., Wang, W., Yang, Y., Fu, R., Cunnold, D., and Choi, Y.: Impact of East Asian
1348 summer monsoon on the air quality over China: view from space, *J. Geophys. Res.*, 115,
1349 D09301, doi:10.1029/2009JD012745, 2010.

1350

1351 Zhao, T. L., Gong, S. L., Zhang, X. Y., and Jaffe, D. A.: Asian dust storm influence on
1352 North American ambient PM levels: observational evidence and controlling factors,
1353 *Atmos. Chem. Phys.*, 8, 2717-2728, doi:10.5194/acp-8-2717-2008, 2008.

1354

1355 Zhou, D., Ding, A., Mao, H., Fu, C., Wang, T., Chan, L. Y., Ding, K., Zhang, Y., Liu, J.,
1356 Lu, A., and Hao, N.: Impacts of the East Asian monsoon on lower tropospheric ozone
1357 over coastal South China, *Environ. Res. Lett.*, 8, 044011,
1358 doi:10.1088/1748-9326/8/4/044011, 2013.

1359
1360

1361 **Figure caption**

1362 Fig. 1. The Degree of Freedom for Signal (DFS) of the MOPITT V5 TIR/NIR data over
1363 East Asia, averaged for 2005 during (a) daytime and (b) nighttime. Locations of four
1364 cities with MOZAIC CO measurements are indicated as stars. Note that the MOZAIC CO
1365 data from Narita also include a small portion of measurements from its surrounding cities
1366 at Osaka and Nagoya.

1367

1368 Fig. 2. Relative bias of CO profiles (in %) between MOPITT and MOZAIC data
1369 (smoothed with the MOPITT averaging kernels, see Equation 1) from 2003 to 2005 at

1370 Beijing, Narita, Shanghai, and Hong Kong for MOPITT V4 and V5 data. The number of
1371 profiles for the comparison is 18, 23, 11, and 15, respectively, at Beijing, Narita,
1372 Shanghai, and Hong Kong. The error bars indicate the interquartile range of the mean.
1373

1374 Fig. 3. Correlation between MOPITT and MOZAIC data (smoothed with the MOPITT
1375 averaging kernels, see Equation 1) from 2003 to 2005 at Beijing, Narita, Shanghai, and
1376 Hong Kong (a) from the middle to upper troposphere and (b) from the surface to the
1377 middle troposphere.
1378

1379 Fig. 4. MOPITT CO mixing ratio (ppbv, in color) (a) on 6 June 2003 at 500 hPa, (b) on
1380 18 March 2004 at 700 hPa, and (c) on April 10, 2005 at 300 hPa. All are overlaid with
1381 horizontal winds (in arrows) at the same altitude. In each subfigure, the geographic
1382 locations of MOZAIC data at 900, 600, and 300 hPa are indicated as red, blue and pink
1383 dots, respectively. The box indicates an area over which mean MOPITT CO profile are
1384 taken and displayed in Fig.5. The box is selected to ensure over 30 MOPITT samplings at
1385 the closest upwind direction of MOZAIC measurements. The two blue dashed lines
1386 define the longitudinal zone, over which the CO abundances were averaged and shown in
1387 Fig 6. The solid blue bars in Figs. 4a and 4c indicate the locations where particles were
1388 released and backward trajectories were simulated using FLEXPART (see text for detail).
1389

1390 Fig. 5. Profiles of MOPITT CO and the a priori, averaged over the corresponding boxed
1391 area in Fig. 4 on (a) 6 June 2003, (c) 18 March 2004, and (e) 10 April 2005, respectively,
1392 along with their monthly mean MOPITT CO profile over the same area. The
1393 corresponding MOZAIC CO profiles (along the dots in Fig. 4) on the same day are
1394 shown in (b), (d), and (f), respectively. The corresponding MOZAIC ozone and relative
1395 humidity profiles are also shown in (b), (d), and (f). Note that the smoothed MOZAIC
1396 CO profiles (MOZAIC CO(s)) were calculated using the averaging kernels and the a
1397 priori in the boxed area in each case (see Sect. 5 for discussion).
1398

1399 Fig. 6. A latitude-altitude cross section of MOPITT CO averaged between the two blue
1400 dashed lines in Fig.4 on (a) June 6, 2003, (b) March 18, 2004, and (c) April 10, 2005. The
1401 contour lines indicate U wind speed (m s^{-1}). Vectors are for wind directions in V and W.
1402 For a better illustration, W is enlarged by a factor of 100. The pink box(es) in (a) and (c)
1403 indicate the locations where particles were released and backward trajectories were
1404 simulated using FLEXPART (see text for detail).
1405

1406 Fig. 7. (a) Particle distribution between 6.25-10.25 km (~550-250 hPa) during June 1-6,
1407 2003. The particles were released from two locations (in pink lines) around 400 hPa (also
1408 see Figs. 4a and 6a) on June 6, 2003 and backward trajectories were calculated. The
1409 contour lines are the geopotential heights at 850 hPa on June 3, 2003. A cold front and a
1410 warm front are indicated by green and red lines, respectively. (b) The same as (a), but
1411 between 0-3.5 km. The contour lines are the geopotential heights at 850 hPa on 2 June
1412 2003. The circles, diamonds, and stars denote daily mean fire counts of 20-100, 100-300,
1413 and 300-500 per $2.5 \times 2.5^\circ$ grid area, respectively, from May 31 to June 6.
1414

1415 Fig. 8. Vertical distribution of particles, varying with time from 1 June 2003 at 0 UTC to

1416 16 June 2003 at 0 UTC. The particles were released from fire regions in Fig. 7b from the
1417 surface to 3 km on 1 June 2003 and forward trajectories were calculated (15 days). The
1418 forward time (in hour) and date (in June) are indicated in the x-axis on the bottom and the
1419 top, respectively.

1420

1421 Fig. 9. MOPITT CO mixing ratio at 700 hPa from 11-19 March 2004, overlaid with the
1422 geopotential height at 850 hPa on 17 March 2004 in blue contour and with a front shown
1423 by brown solid line. The large and small stars denote daily mean fire counts of 100-200
1424 and over 200 per $2.5 \times 2.5^\circ$ grid area during the period, respectively. “L” and “H” indicate
1425 a low and high pressure system, respectively.

1426

1427 Fig. 10. (a) CO, (b) CO from biomass burning, and (c) CO from the anthropogenic source
1428 on March 18, 2004 at 0 UTC, simulated by GEOS-Chem. The geopotential height at 700
1429 hPa is indicated with white lines. “L” indicates a low pressure system.

1430

1431 Fig. 11. Latitude-altitude cross sections along 130°E of (a) CO, (b) CO from biomass
1432 burning, and (c) anthropogenic CO on March 17, 2004 at 6 UTC, simulated by
1433 GEOS-Chem. The contour lines indicate U wind speed (m s^{-1}). Vectors are for wind
1434 directions in V and W. For a better illustration, W is enlarged by a factor of 100.

1435

1436 Fig. 12. A longitude-altitude cross section of CO along 22°N on March 17, 2004 at 6
1437 UTC, simulated by GEOS-Chem. The topography of the Hengduan Mountains is
1438 indicated in white.

1439

1440 Fig. 13. MOPITT CO mixing ratio at 800 hPa from April 3-10, 2005, overlaid with the
1441 geopotential height at 850 hPa on April 9, 2005 at 0 UTC in blue contour and with a front
1442 in brown solid line. The large and small stars denote daily mean fire counts of 100-200
1443 and over 200 per $2.5 \times 2.5^\circ$ grid area during the period, respectively. The boxed area was
1444 identified as a major CO source region from the FLEXPART simulation (see text for
1445 detail).

1446

1447 Fig. 14. The GEOS-Chem simulated CO (a) on April 8, 2005 in the lower troposphere
1448 (800-700 hPa), (b) on April 9 in the middle troposphere (500-400 hPa), and (c) on April
1449 10 in the upper troposphere (300-200 hPa). The contours are the geopotential height at
1450 850, 450, and 250 hPa, respectively.

1451

1452 Fig. 15. The GEOS-Chem simulated fractional CO (a) from biomass burning and (b)
1453 from the anthropogenic source on April 10, 2005 at 00 UTC in the middle troposphere
1454 (500-400 hPa). (c) and (d) are the same as for (a) and (b), respectively, but in the upper
1455 troposphere (300-200 hPa). The geopotential height at 450 and 250 hPa is overlaid with
1456 the CO images in the middle and upper troposphere, respectively. White dots indicate the
1457 location of MOZAIC measurements.

1458

1459 **Table caption**

1460 **Table 1.** Characterization of the three cases.

1461

1462 **Table 2.** Occurrences of various CO ranges at different altitudes in the MOZAIC
1463 measurements in the vicinity of Narita from 2001 to 2006.

1464

1465 **Table 3.** Occurrences of various CO ranges at different altitudes in GEOS-Chem
1466 simulations and MOPITT observations in the vicinity of Narita (126-140 °E 30-40 °N) in
1467 2005.

1468

1469

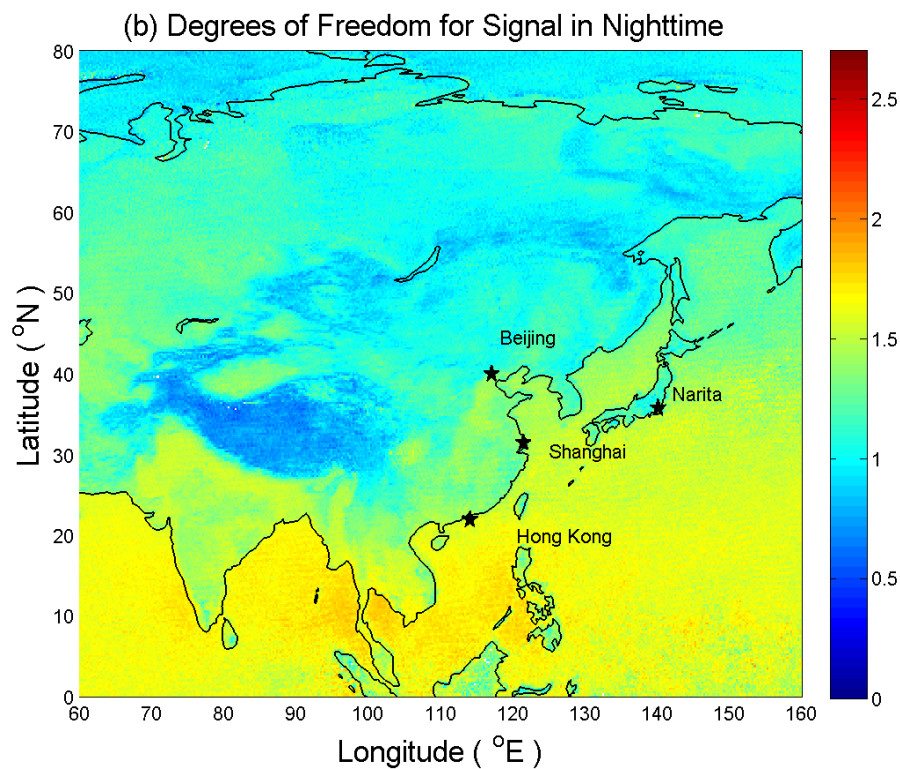
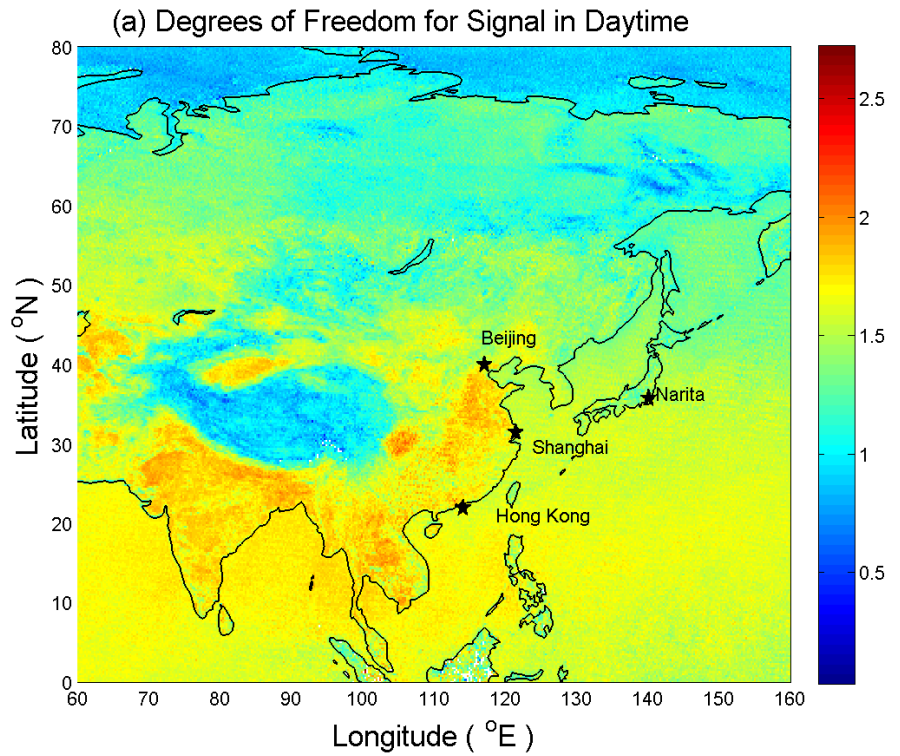


Fig. 1. The Degree of Freedom for Signal (DFS) of the MOPITT V5 TIR/NIR data over East Asia, averaged for 2005 during (a) daytime and (b) nighttime. Locations of four cities with MOZAIC CO measurements are indicated as stars. Note that the MOZAIC CO data from Narita also include a small portion of measurements from its surrounding cities at Osaka and Nagoya.

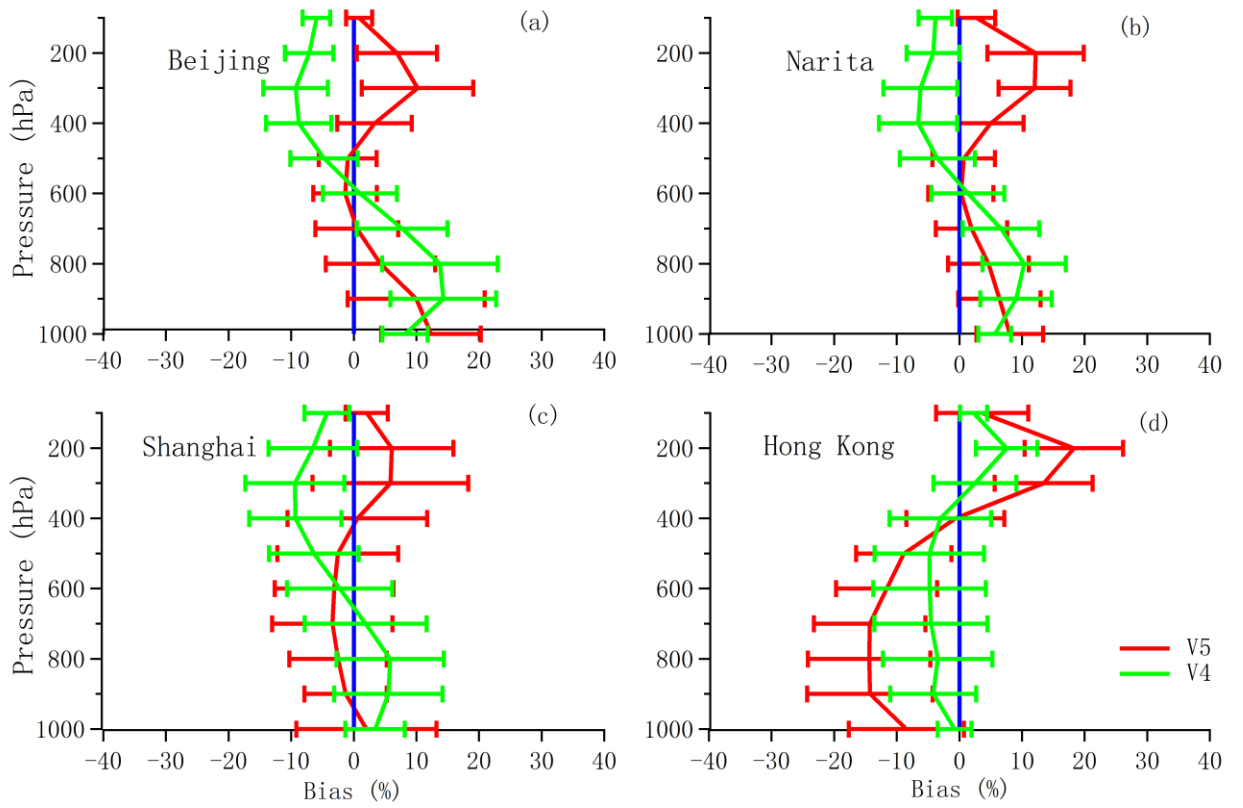


Fig. 2. Relative bias of CO profiles between MOPITT and MOZAIC data (smoothed with the MOPITT averaging kernels, see Equation 1) from 2003 to 2005 at Beijing, Narita, Shanghai, and Hong Kong for MOPITT V4 and V5 data. The number of profiles for the comparison is 18, 23, 11, and 15, respectively, at Beijing, Narita, Shanghai, and Hong Kong. The error bars indicate the interquartile range of the mean.

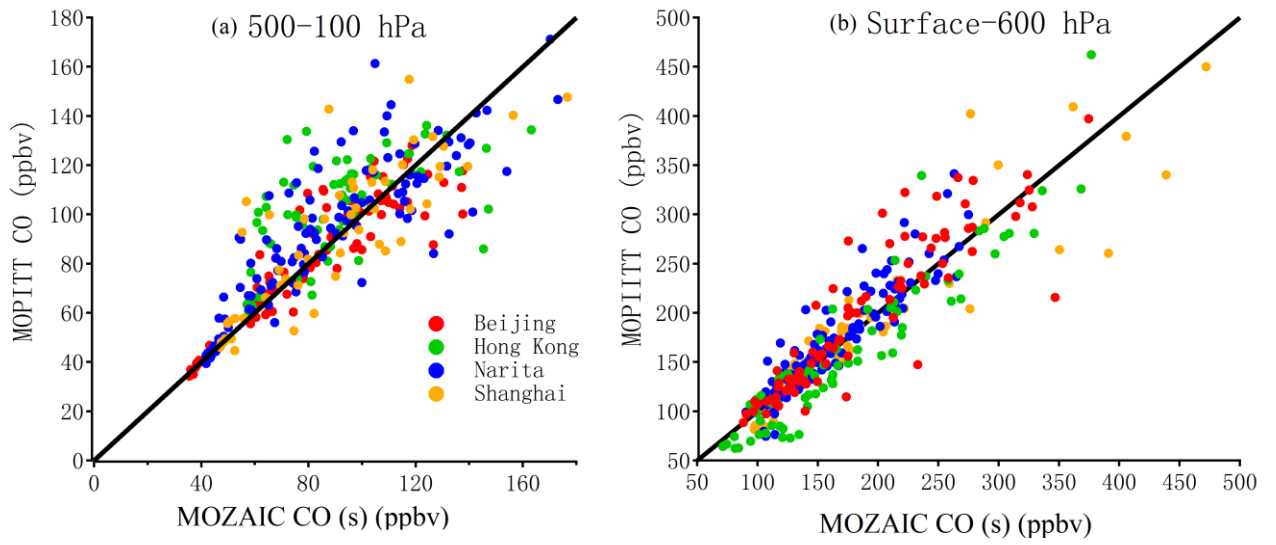
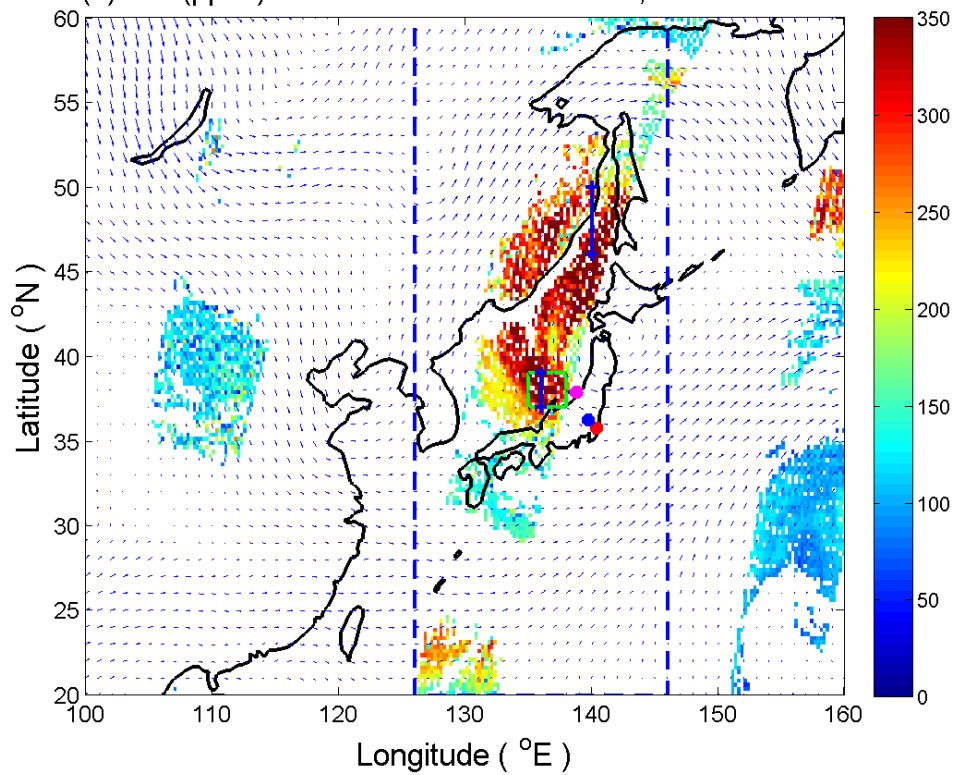
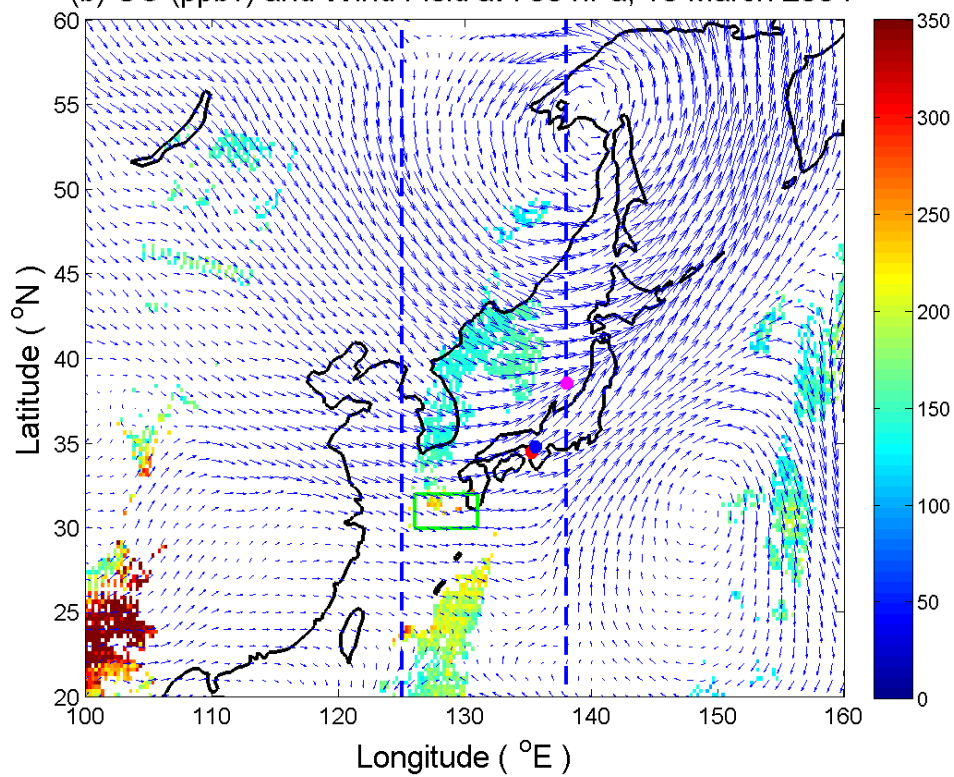


Fig. 3. Correlation between MOPITT and MOZAIC data (smoothed with the MOPITT averaging kernels, see Equation 1) from 2003 to 2005 at Beijing, Narita, Shanghai, and Hong Kong (a) from the middle to upper troposphere and (b) from the surface to the middle troposphere.

(a) CO (ppbv) and Wind Field at 500 hPa, 06 June 2003



(b) CO (ppbv) and Wind Field at 700 hPa, 18 March 2004



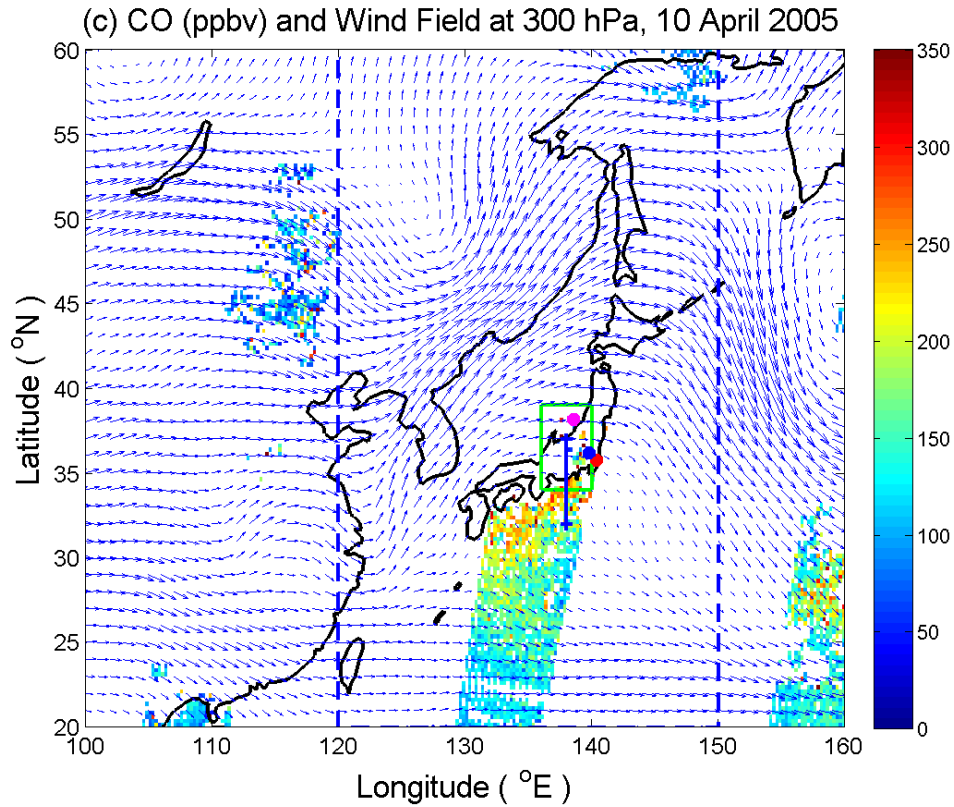
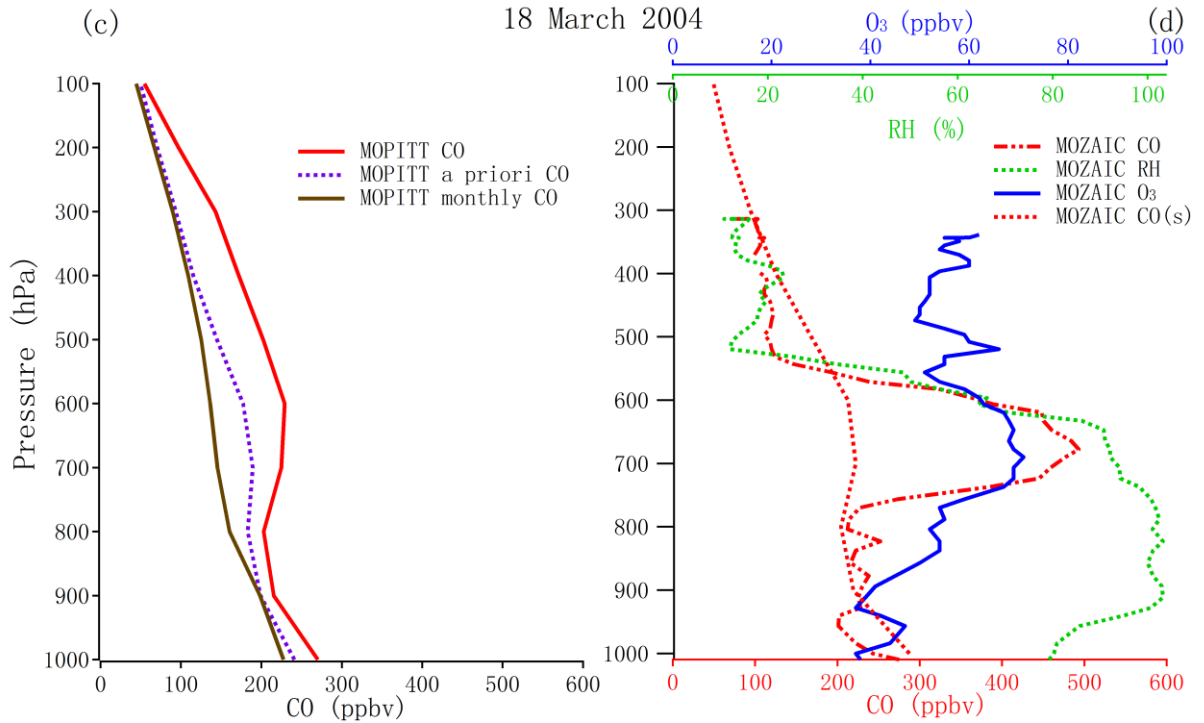
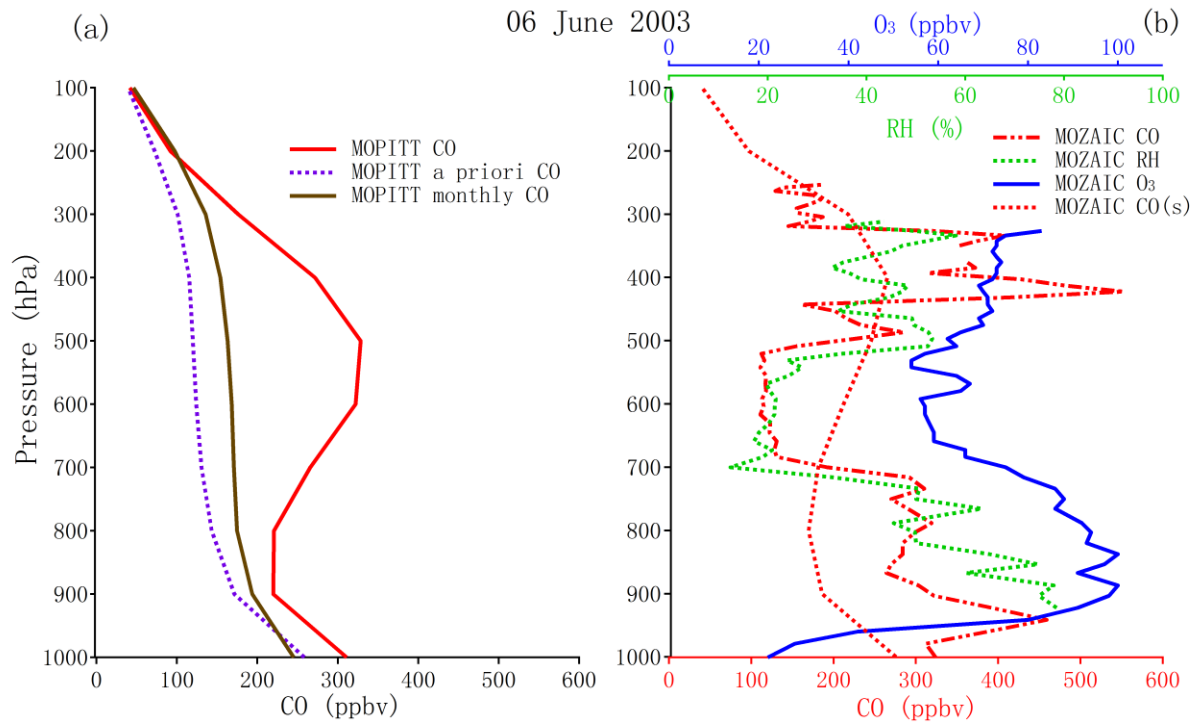


Fig. 4. MOPITT CO mixing ratio (ppbv, in color) (a) on 6 June 2003 at 500 hPa, (b) on 18 March 2004 at 700 hPa, and (c) on April 10, 2005 at 300 hPa. All are overlaid with horizontal winds (in arrows) at the same altitude. In each subfigure, the geographic locations of MOZAIC data at 900, 600, and 300 hPa are indicated as red, blue and pink dots, respectively. The box indicates an area over which mean MOPITT CO profile are taken and displayed in Fig.5. The box is selected to ensure over 30 MOPITT samplings at the closest upwind direction of MOZAIC measurements. The two blue dashed lines define the longitudinal zone, over which the CO abundances were averaged and shown in Fig. 6. The solid blue bars in Figs. 4a and 4c indicate the locations where particles were released and backward trajectories were simulated using FLEXPART (see text for detail).



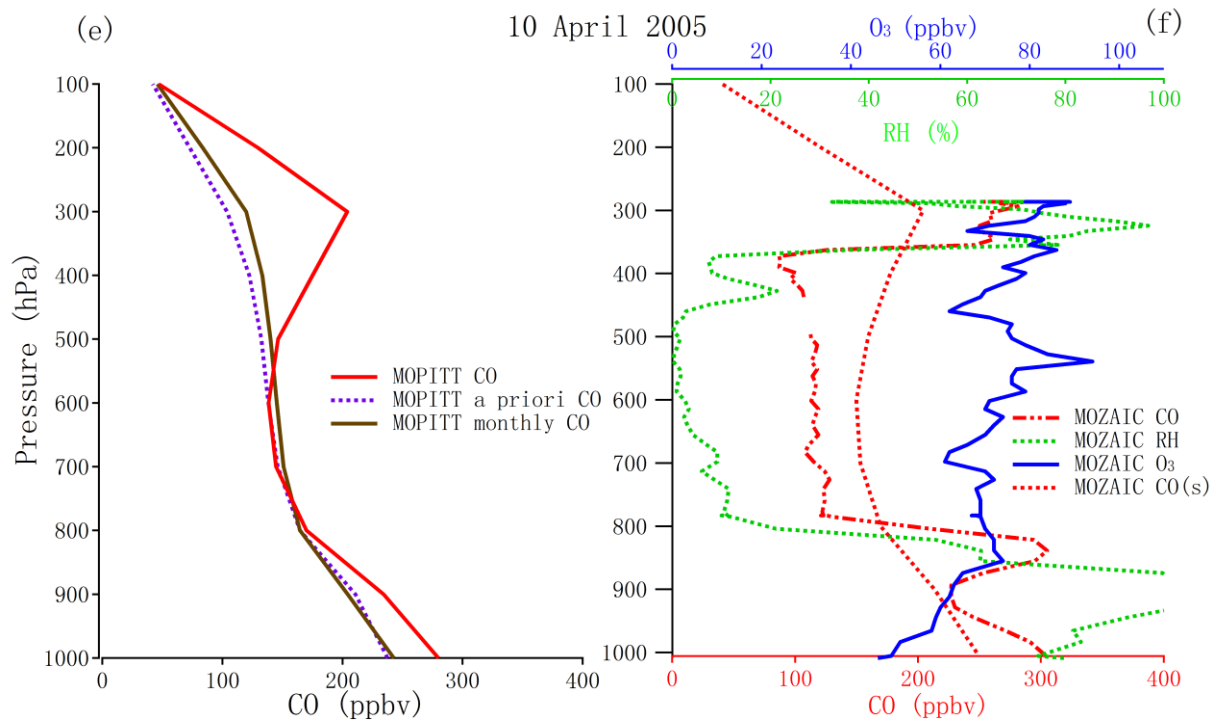
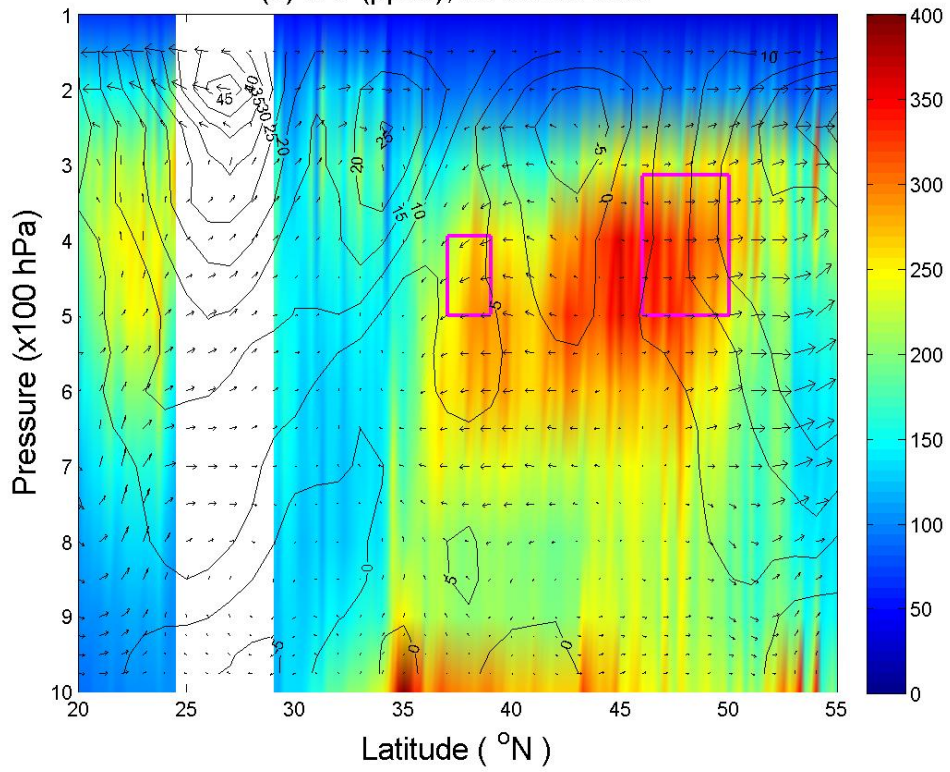
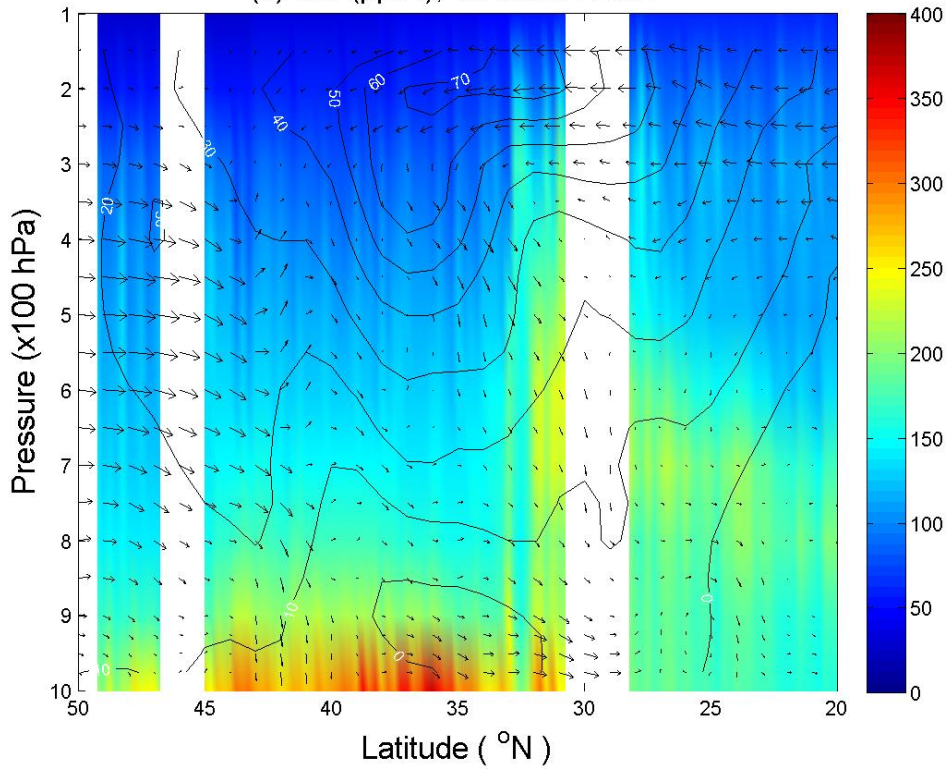


Fig. 5. Profiles of MOPITT CO and the a priori, averaged over the corresponding boxed area in Fig. 4 on (a) 6 June 2003, (c) 18 March 2004, and (e) 10 April 2005, respectively, along with their monthly mean MOPITT CO profile over the same area. The corresponding MOZAIC CO profiles (along the dots in Fig. 4) on the same day are shown in (b), (d), and (f), respectively. The corresponding MOZAIC ozone and relative humidity profiles are also shown in (b), (d), and (f). Note that the smoothed MOZAIC CO profiles (MOZAIC CO(s)) were calculated using the averaging kernels and the a priori in the boxed area in each case (see Sect. 5 for discussion).

(a) CO (ppbv), 06 June 2003



(b) CO (ppbv), 18 March 2004



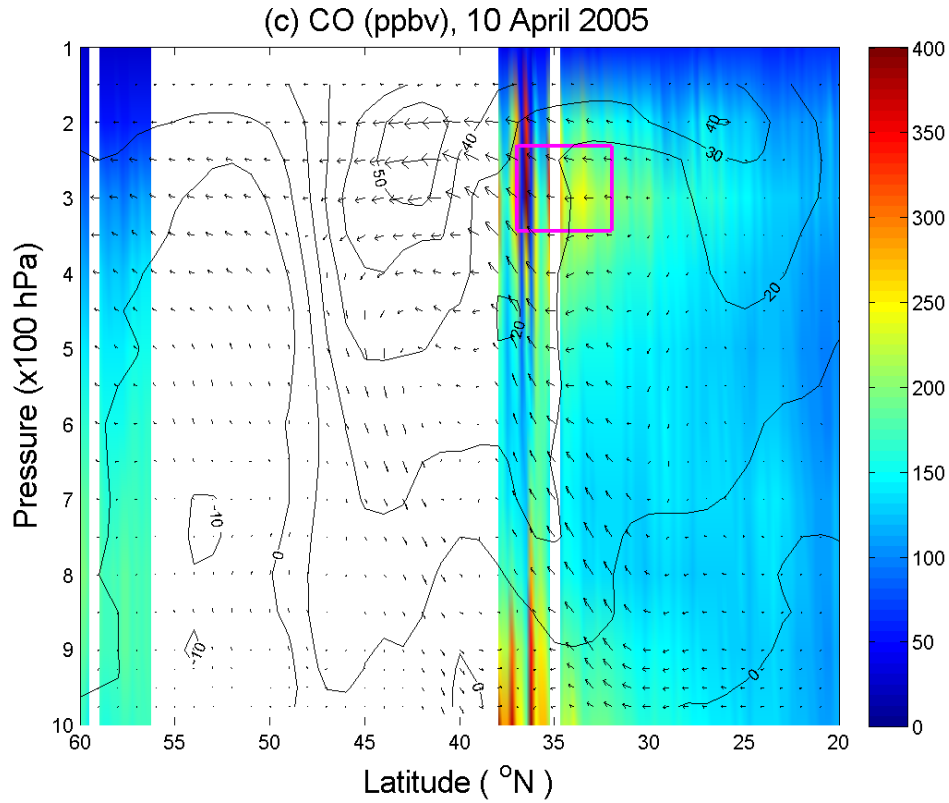
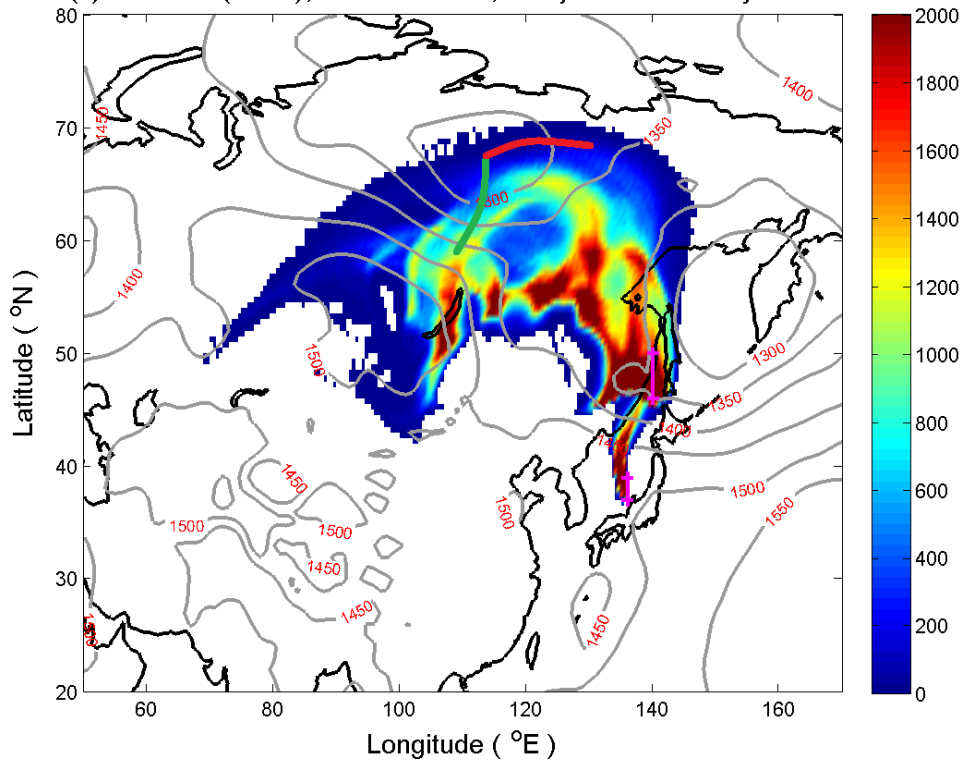


Fig. 6. A latitude-altitude cross section of MOPITT CO averaged between the two blue dashed lines in Fig.4 on (a) June 6, 2003, (b) March 18, 2004, and (c) April 10, 2005. The contour lines indicate U wind speed (m s^{-1}). Vectors are for wind directions in V and W. For a better illustration, W is enlarged by a factor of 100. The pink box(es) in (a) and (c) indicate the locations where particles were released and backward trajectories were simulated using FLEXPART (see text for detail).

(a) Particles (count), 6.25-10.25 km, 5-day Backward Trajectories



(b) Particles (count), 0-3.25 km, 5-day Backward Trajectories

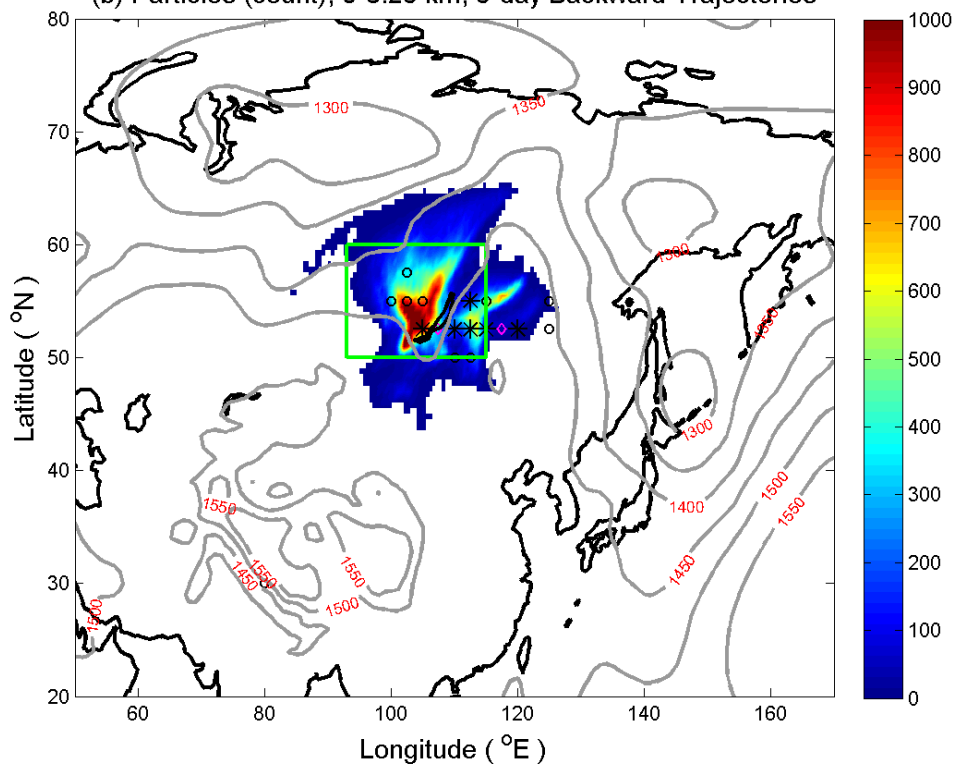


Fig. 7. (a) Particle distribution between 6.25-10.25 km (~550-250 hPa) during June 1-6, 2003. The particles were released from two locations (in pink lines) around 400 hPa (also see Figs. 4a and 6a) on June 6, 2003 and backward trajectories were calculated. The contour lines are the geopotential heights at 850 hPa on June 3, 2003. A cold front and a warm front are indicated by green and red lines, respectively. (b) The same as (a), but between 0-3.5 km. The contour lines are the geopotential heights at 850 hPa on 2 June 2003. The circles, diamonds, and stars denote daily mean fire counts of 20-100, 100-300, and 300-500 per $2.5 \times 2.5^\circ$ grid area, respectively, from May 31 to June 6.

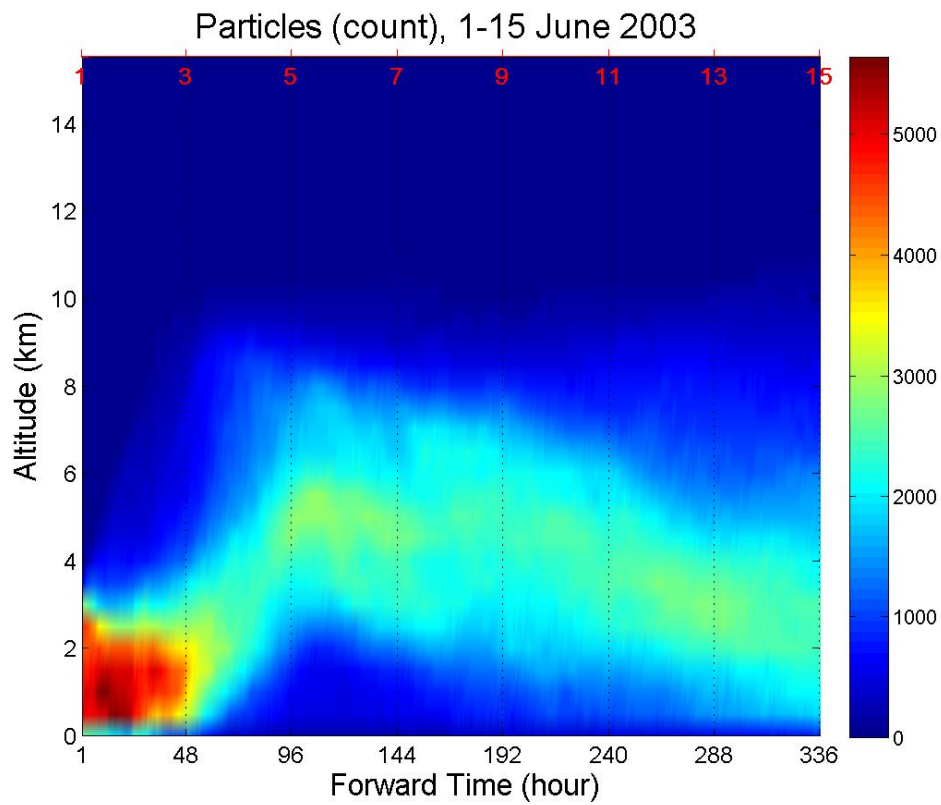


Fig. 8. Vertical distribution of particles, varying with time from 1 June 2003 at 0 UTC to 16 June 2003 at 0 UTC. The particles were released from fire regions in Fig. 7b from the surface to 3 km on 1 June 2003 and forward trajectories were calculated (15 days). The forward time (in hour) and date (in June) are indicated in the x-axis on the bottom and the top, respectively.

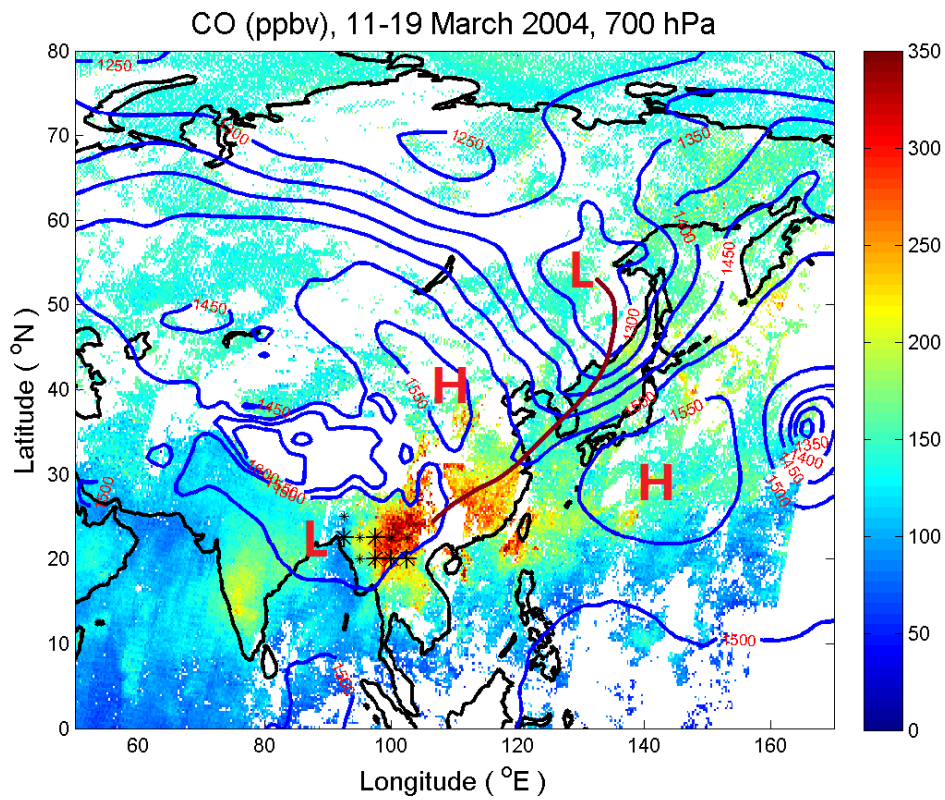


Fig. 9. MOPITT CO mixing ratio at 700 hPa from 11-19 March 2004, overlaid with the geopotential height at 850 hPa on 17 March 2004 in blue contour and with a front shown by brown solid line. The large and small stars denote daily mean fire counts of 100-200 and over 200 per $2.5 \times 2.5^\circ$ grid area during the period, respectively. “L” and “H” indicate a low and high pressure system, respectively.

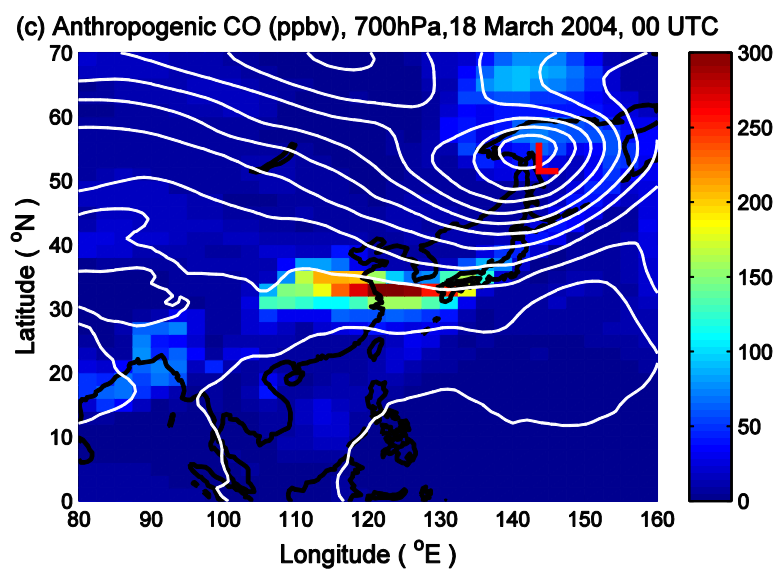
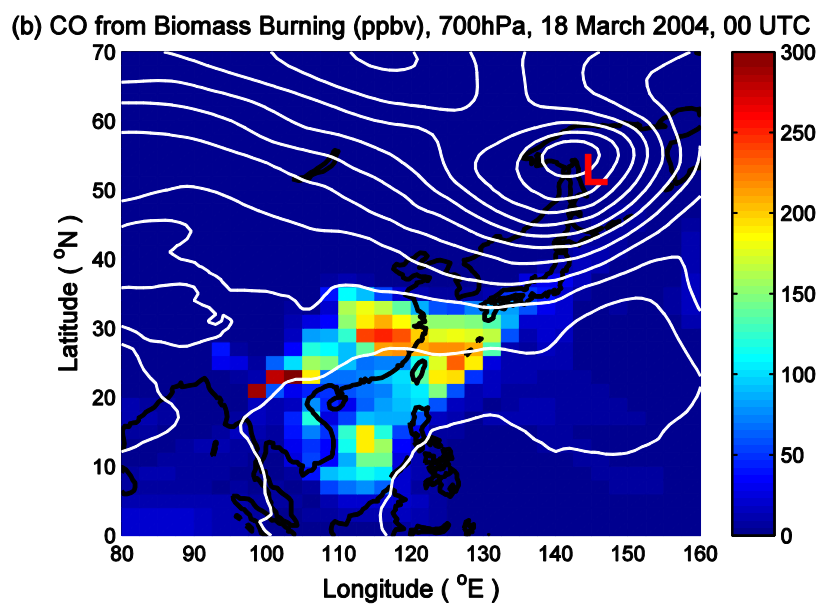
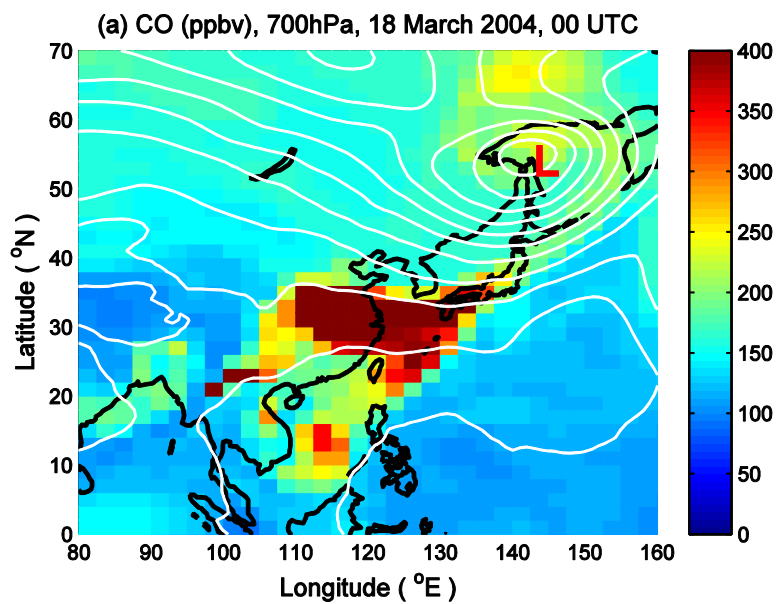
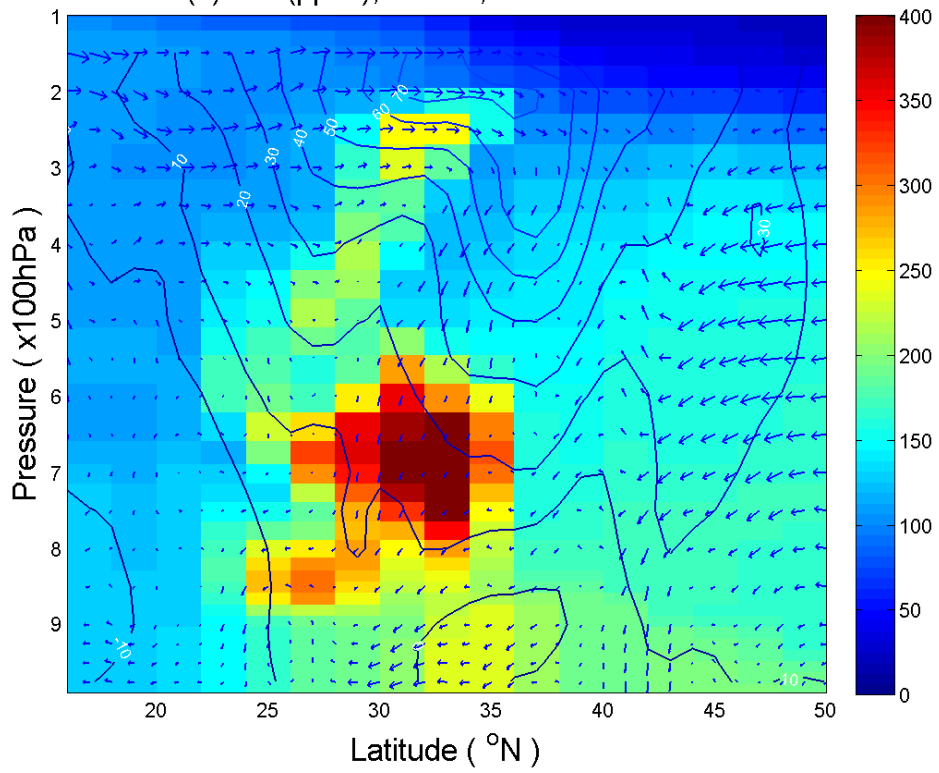
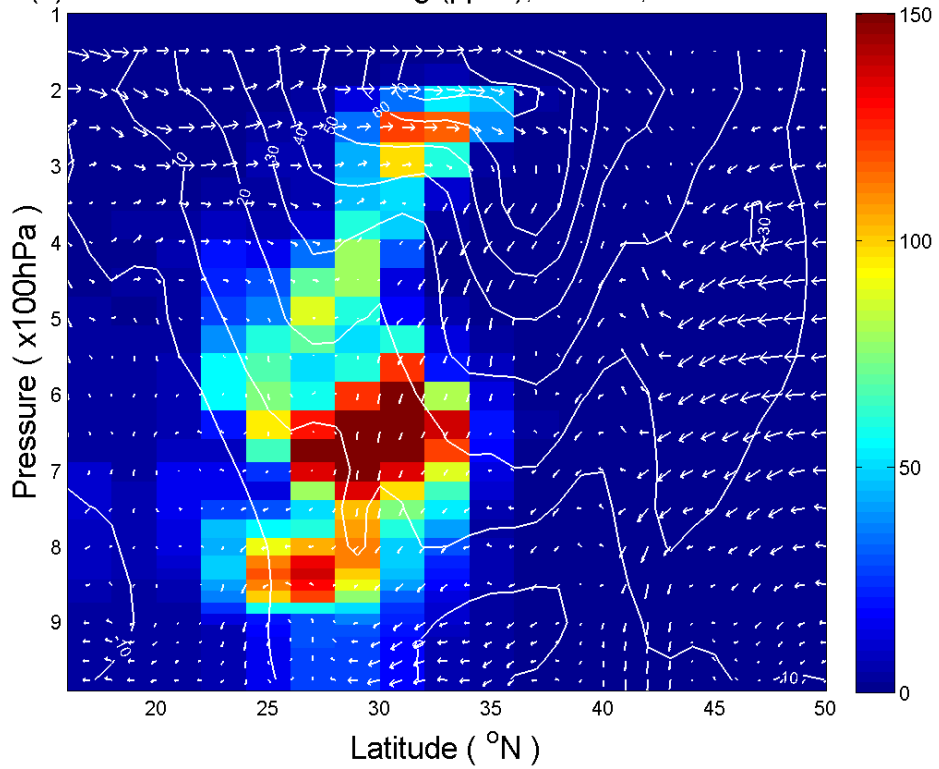


Fig. 10. (a) CO, (b) CO from biomass burning, and (c) CO from the anthropogenic source on March 18, 2004 at 0 UTC, simulated by GEOS-Chem. The geopotential height at 700 hPa is indicated with white lines. “L” indicates a low pressure system.

(a) CO (ppbv), 130°E, 18 March 2004



(b) CO from Biomass Burning (ppbv), 130°E, 18 March 2004



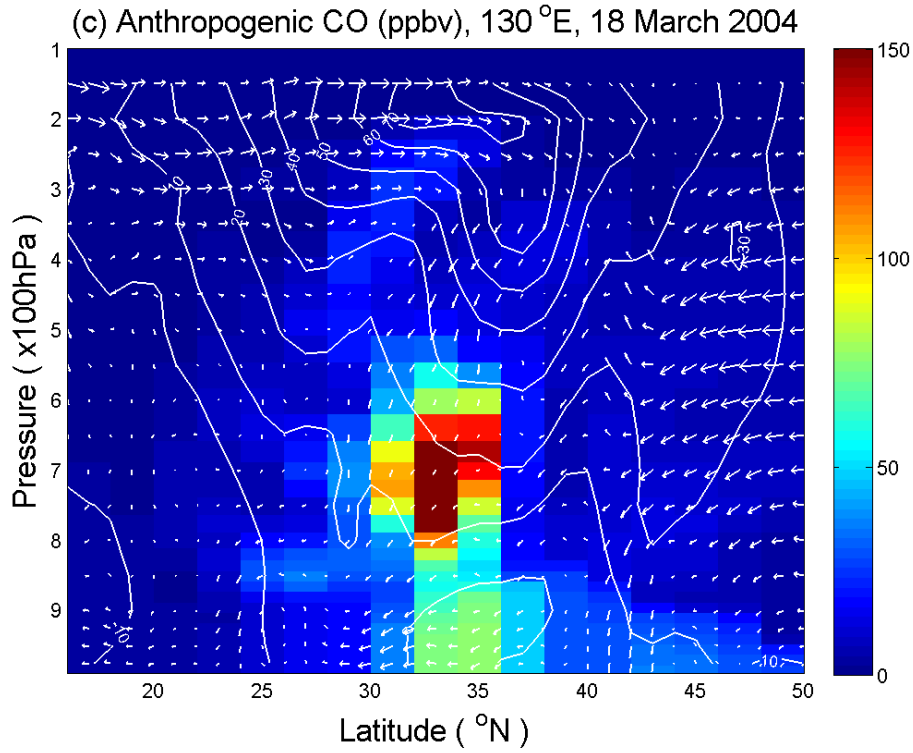


Fig. 11. Latitude-altitude cross sections along 130°E of (a) CO, (b) CO from biomass burning, and (c) anthropogenic CO on March 17, 2004 at 6 UTC, simulated by GEOS-Chem. The contour lines indicate U wind speed (m s^{-1}). Vectors are for wind directions in V and W. For a better illustration, W is enlarged by a factor of 100.

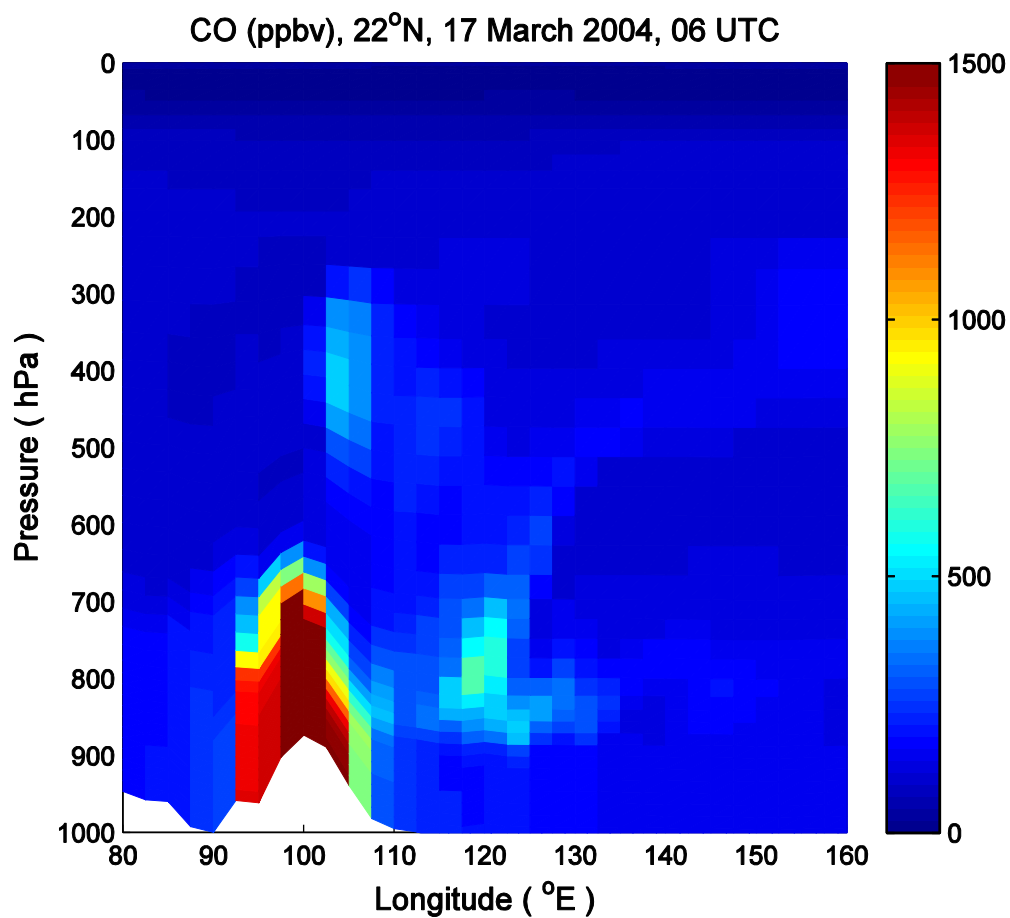


Fig. 12. A longitude-altitude cross section of CO along 22°N on March 17, 2004 at 6 UTC, simulated by GEOS-Chem. The topography of the Hengduan Mountains is indicated in white.

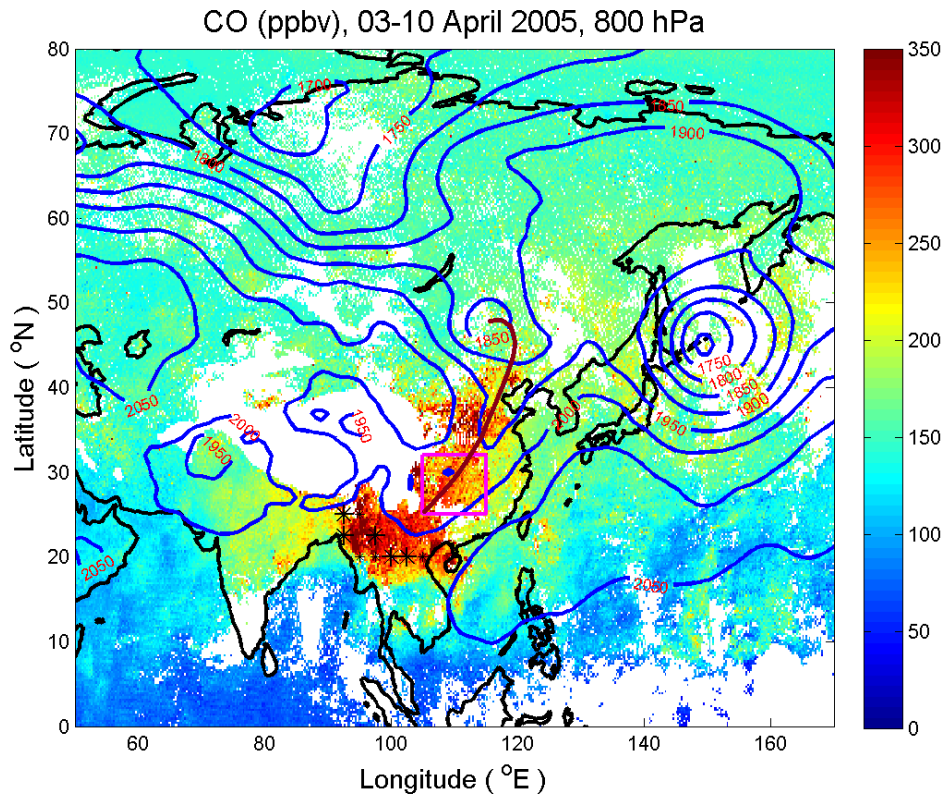
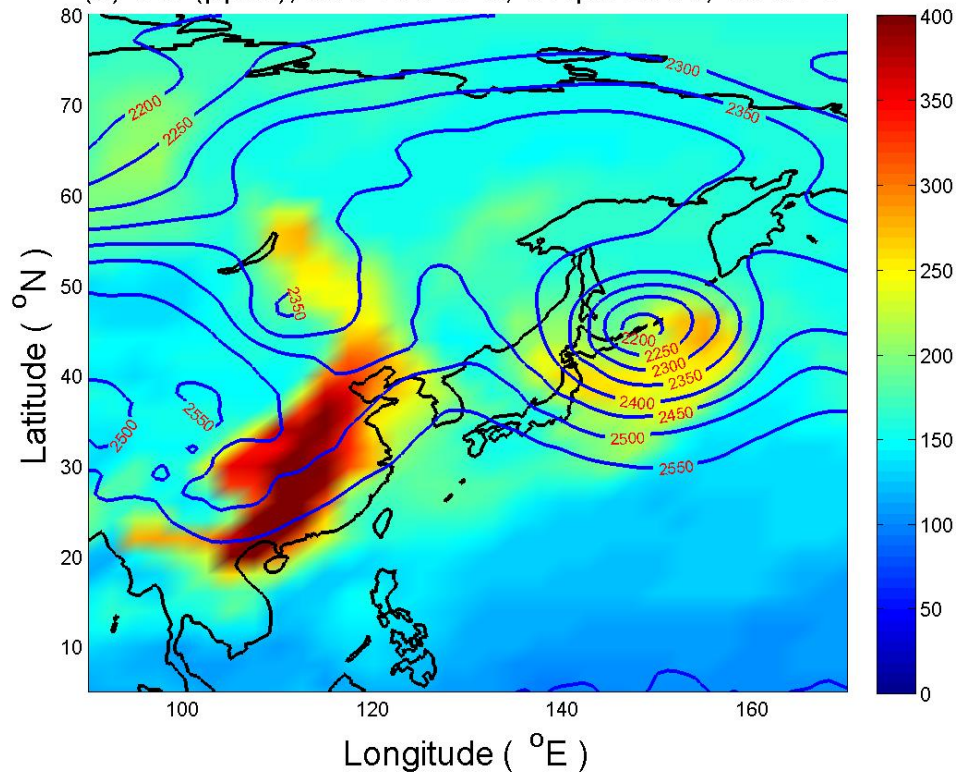
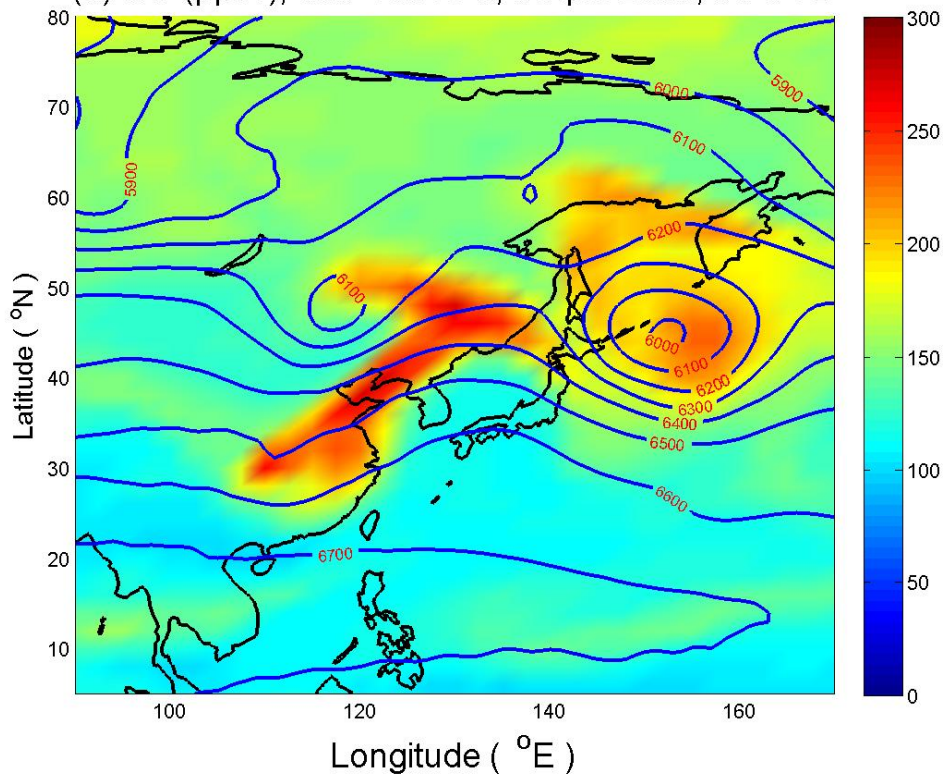


Fig. 13. MOPITT CO mixing ratio at 800 hPa from April 3-10, 2005, overlaid with the geopotential height at 850 hPa on April 9, 2005 at 0 UTC in blue contour and with a front in brown solid line. The large and small stars denote daily mean fire counts of 100-200 and over 200 per $2.5 \times 2.5^\circ$ grid area during the period, respectively. The boxed area was identified as a major CO source region from the FLEXPART simulation (see text for detail).

(a) CO (ppbv), 800-700 hPa, 8 April 2005, 18 UTC



(b) CO (ppbv), 500-400 hPa, 9 April 2005, 06 UTC



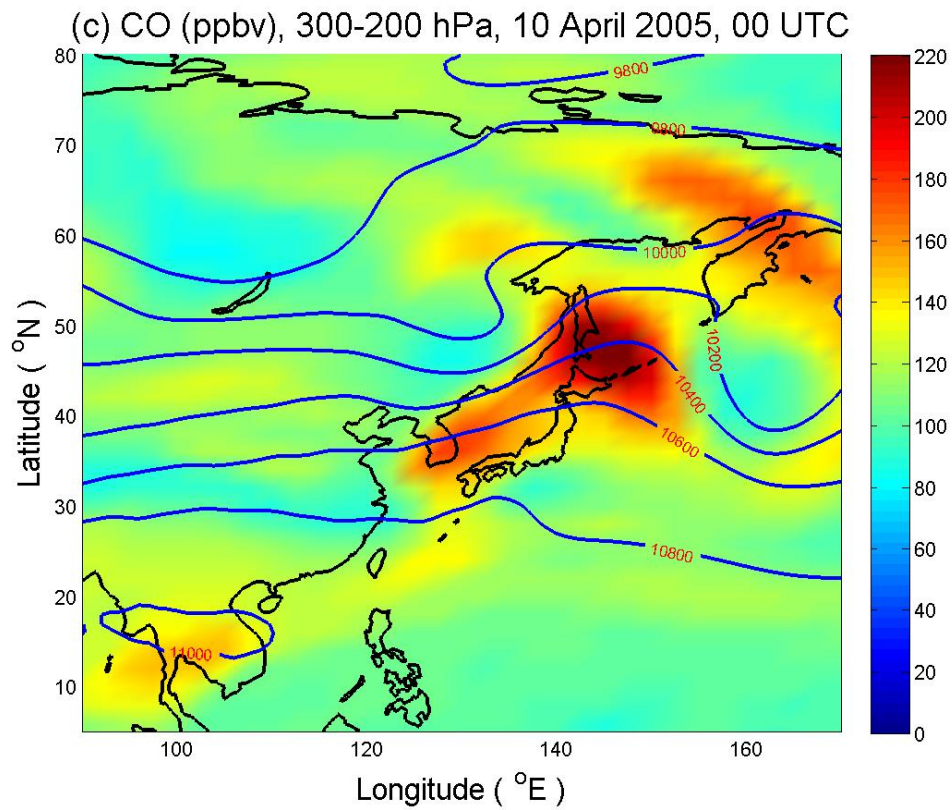
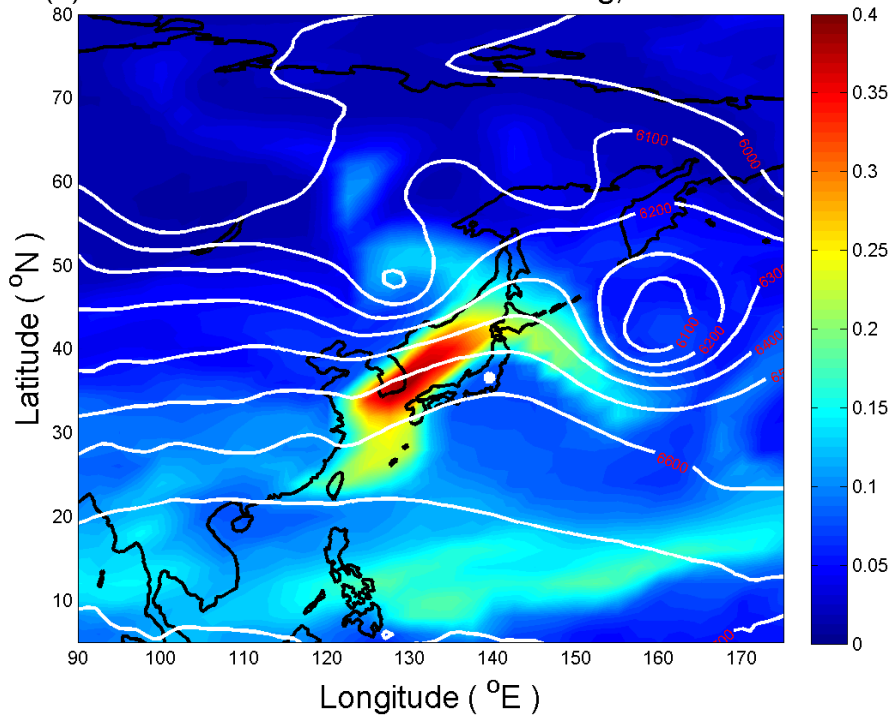
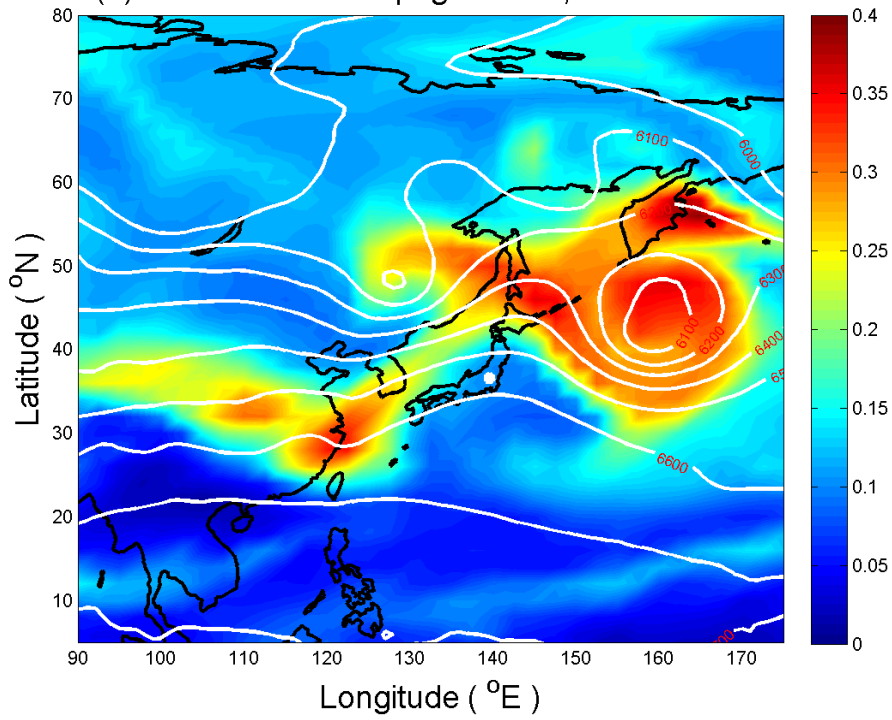


Fig. 14. The GEOS-Chem simulated CO (a) on April 8, 2005 in the lower troposphere (800-700 hPa), (b) on April 9 in the middle troposphere (500-400 hPa), and (c) on April 10 in the upper troposphere (300-200 hPa). The contours are the geopotential height at 850, 450, and 250 hPa, respectively.

(a) Fraction of CO from Biomass Burning, 500-400 hPa



(b) Fraction of Anthropogenic CO, 500-400 hPa



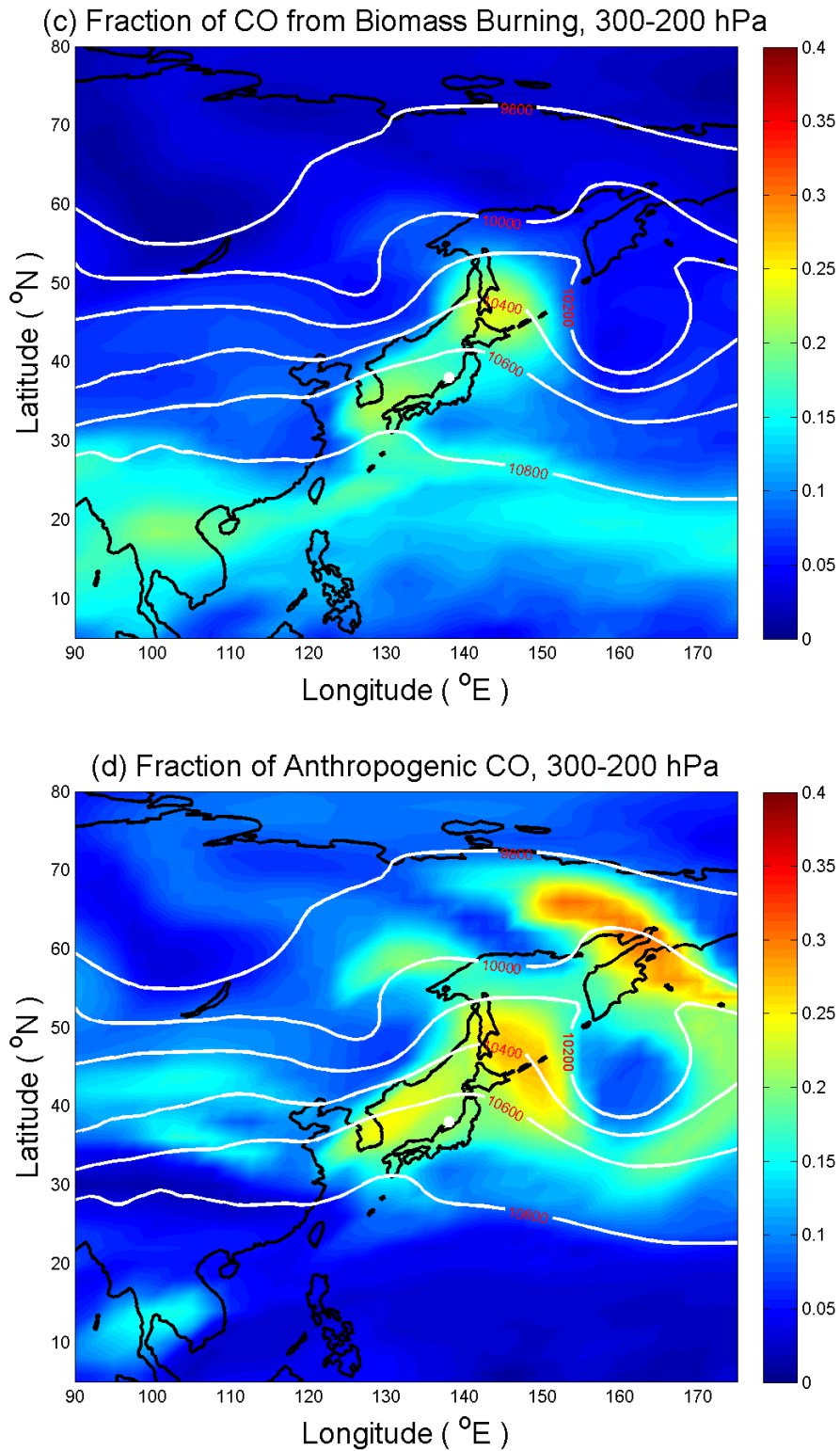


Fig. 15. The GEOS-Chem simulated fractional CO (a) from biomass burning and (b) from the anthropogenic source on April 10, 2005 at 00 UTC in the middle troposphere (500-400 hPa). (c) and (d) are the same as for (a) and (b), respectively, but in the upper troposphere (300-200 hPa). The geopotential height at 450 and 250 hPa is overlaid with the CO images in the middle and upper troposphere, respectively. White dots indicate the location of MOZAIC measurements.

Table 1. Characterization of the three cases.

Case	2003	2004	2005
Date	6 June 2003	18 March 2004	10 April 2005
Maximum CO (ppbv) in MOZAIC profiles in FT	~550	~500	~300
CO peak height (hPa) in MOZAIC profiles in FT	500-300	750-550	350-250
Maximum CO (ppbv) in MOPITT images	300-400	200-250	150-200
CO peak height (hPa) in MOPITT images	650-300	750-500	400-250
Peak CO area in MOPITT images	35-55°N 125-145°E	20-32°N 125-135°E	32-37°N 130-140°E
Major CO sources	Large fires near Lake Baikal in Russia	Fires in the Indochina peninsula, anthropogenic emissions in the North China Plain	Fires in the Indochina peninsula, anthropogenic emissions in the North China Plain and the Sichuan basin
Vertical transport mechanism	Frontal lifting	Convection (due to leeside troughs), frontal lifting, and orographic lifting	Convection, frontal lifting
Outflow	West coast of Canada	West coast of the United States	West coast of Canada

Table 2. Occurrences of various CO ranges at different altitudes in the MOZAIC measurements in the vicinity of Narita from 2001 to 2006.

Season	Pressure (hPa)	Occurrence						Fractional Occurrence (%)					
		CO Concentration Range (ppbv)						CO Concentration Range (ppbv)					
		0-100	100-200	200-300	300-400	>400	All	0-100	100-200	200-300	300-400	>400	All
All	400-200	67	354	93	19	6	539	12	66	17	4	1	100
	600-400	36	359	69	15	8	487	7	74	14	3	2	100
	850-600	17	180	150	31	6	384	4	47	39	8	2	100
	Surface-850	4	60	142	83	88	377	1	16	38	22	23	100
Spring	400-200	11	96	28	12	2	149	7	64	19	8	1	100
	600-400	1	101	29	9	3	143	1	71	20	6	2	100
	850-600	0	38	55	20	5	118	0	32	47	17	4	100
	Surface-850	0	14	44	27	29	114	0	12	39	24	25	100
Summer	400-200	14	132	41	4	4	195	7	68	21	2	2	100
	600-400	13	138	22	1	2	176	7	78	13	1	1	100
	850-600	14	80	50	6	0	150	9	53	33	4	0	100
	Surface-850	4	32	48	30	36	150	3	21	32	20	24	100
Fall	400-200	30	61	15	2	0	108	28	56	14	2	0	100
	600-400	20	50	11	2	1	84	24	60	13	2	1	100
	850-600	3	30	17	3	0	53	6	57	32	6	0	100
	Surface-850	0	10	20	12	11	53	0	19	38	23	21	100
Winter	400-200	12	65	9	1	0	87	14	75	10	1	0	100
	600-400	2	70	7	3	2	84	2	83	8	4	2	100
	850-600	0	32	28	2	1	63	0	51	44	3	2	100
	Surface-850	0	4	30	14	12	60	0	7	50	23	20	100

Table 3. Occurrences of various CO ranges at different altitudes in GEOS-Chem simulations and MOPITT observations in the vicinity of Narita (126-140 °E 30-40 °N) in 2005.

Pressure (hPa)	GEOS-Chem: Fractional Occurrence (%)						Pressure (hPa)	MOPITT: Fractional Occurrence (%)				
	0-100	100-200	200-300	300-400	>400	All		0-100	100-200	200-250	>250	All
200-100	12	87	1	0	0	100	200-100	38	45	11	6	100
400-200	0	87	12	1	0	100	400-200	4	68	18	10	100
600-400	0	53	35	11	1	100	600-400	6	86	6	1	100
850-600	0	20	46	25	8	100	800-600	7	67	20	6	100
1000-850	0	7	46	35	11	100	1000-800	2	16	18	64	100